A&A, 712, A92 (2026)
https://doi.org/10.1051/0004-6361/202557735

Astronomy & Astrophysics

Resolving stellar populations, star formation, and interstellar medium conditions with JWST in a large spiral galaxy at $z \approx 2$

Eleonora Parlanti[1,2,⋆,⋆⋆], Giulia Tozzi[1,⋆,⋆⋆], Natascha M. Förster Schreiber[1], Claudia Pulsoni[1], Letizia Scaloni[1,3,4], Stavros Pastras[1,5], Pascal Oesch[6,7], Capucine Barfety[1], Francesco Belfiore[8], Jianhang Chen[1], Giovanni Cresci[9], Ric Davies[1], Frank Eisenhauer[1,10], Juan M. Espejo Salcedo[1], Reinhard Genzel[1,11], Rodrigo Herrera-Camus[12], Jean-Baptiste Jolly[1], Lilian L. Lee[1], Minju M. Lee[7,13], Daizhong Liu[14], Dieter Lutz[1], Filippo Mannucci[9], Giovanni Mazzolari[1], Thorsten Naab[5], Amit Nestor Shachar[15], Sedona H. Price[16], Alvio Renzini[17], T. Taro Shimizu[1], Amiel Sternberg[15], Martina Scialpi[1,18,19,9], Eckhard Sturm[1], Linda J. Tacconi[1], Hannah Übler[1], and Stijn Wuyts[20]

(Affiliations can be found after the references)

Received 17 October 2025 / Accepted 27 April 2026

ABSTRACT

Cosmic noon represents the prime epoch where today's massive galaxies assembled most of their stellar masses, and it is an ideal period for observations with both the space-based *James Webb Telescope* (JWST) and ground-based near-IR integral-field unit (IFU) spectrographs. This work analyzes JWST NIRSpec Micro Shutter Array (MSA) and NIRCam Wide Field Slitless Spectroscopy (WFSS) observations of K20-ID7, a large spiral, star-forming (SF) galaxy at $z = 2.224$ with evidence of radial gas inflows. Leveraging ground-based IFU ERIS observations, we conducted a comprehensive and resolved study of the interstellar medium and stellar properties of this galaxy, covering the rest-frame optical to near-IR. Our analysis – using several emission-line diagnostics, resolved spectral energy distribution (SED) fitting of high-resolution imaging, and Paβ line detection in NIRCam WFSS data – reveals massive SF clumps ($M_\star \simeq (0.67{-}3.5) \times 10^9\,M_\odot$) with star formation rates (SFRs) of 3–24 $M_\odot\,yr^{-1}$, low dust attenuation ($A_V \simeq 0.4$), electron densities ($n_e \lesssim 300\,cm^{-3}$), and ionization parameter ($\log(U) \simeq -3.0$). The central bulge is modestly massive ($M_\star = (7 \pm 3) \times 10^9\,M_\odot$), heavily obscured ($A_V = 6.43 \pm 0.55$), and likely formed most of its stellar mass in the past (SFR = $82 \pm 42\,M_\odot\,yr^{-1}$ over the last ∼100 Myr). Yet, it continues to form stars at a lower rate (SFR = $12 \pm 8\,M_\odot\,yr^{-1}$ over the last ∼10 Myr). We infer a relatively low sulfur abundance of $\log(S/O) \simeq -1.9$, which may have implications for sulfur production via type I supernova explosions. Moreover, all distinct galaxy regions feature a metallicity of $12+\log(O/H) \approx 8.54$, likely due – along with the enhanced N/O abundance (i.e., $\log(N/O) \simeq -1.0$) – to dilution effects from radial inflows of metal-poor gas. Lastly, we find tentative evidence of a negative gradient in stellar age, suggesting possible inside-out growth for K20-ID7.

Key words. ISM: abundances – galaxies: high-redshift – galaxies: ISM – galaxies: star formation

1. Introduction

Present-day massive galaxies assembled half their current mass at $z \sim 1{-}3$ – the so-called "cosmic noon" epoch – when the star formation rate (SFR) density of the Universe reached its peak ($z \approx 2$; Madau & Dickinson 2014), due to the large amount of available gas (Tacconi et al. 2020; Walter et al. 2020). At this epoch, gas-rich, turbulent star-forming disks represent the bulk of the massive main-sequence galaxy population (Förster Schreiber & Wuyts 2020). These galaxies commonly feature central compact bulges, accreting black holes, galactic winds, and giant star-forming complexes on kiloparsec scales (Genzel et al. 2011, 2014; Wuyts et al. 2012, 2013; Lang et al. 2014; Tacchella et al. 2018; Förster Schreiber et al. 2018, 2019; Ferreira et al. 2023; Espejo Salcedo et al. 2025b; Kalita et al. 2025). Star-forming galaxies at $z \approx 2$ represent a perfect laboratory for probing how galaxies grow and self-regulate and for investigating the origin of the tight scaling relations between the global properties of star-forming galaxies observed in the local Universe and up to high redshifts (e.g., Speagle et al. 2014; Maiolino & Mannucci 2019).

While *James Webb Space Telescope* (JWST) observations have mostly focused on the $z > 4$ Universe – yielding extraordinary discoveries and new questions (e.g., Finkelstein et al. 2023; Curtis-Lake et al. 2023; Carniani et al. 2024; Naidu et al. 2026) – cosmic noon remains the key epoch to explore for ultimately addressing the processes driving galaxy evolution. Unlike $z > 4$, $z \approx 2$ offers a unique advantage: it is an ideal redshift for both JWST and ground-based near-IR integral-field unit (IFU) observations with adaptive optics (AOs), such as SINFONI (Spectrograph for INtegral Field Observations in the Near Infrared; Eisenhauer et al. 2003) and its successor ERIS (Enhanced Resolution Imager and Spectrograph; Davies et al. 2023) at the Very Large Telescope (VLT). While near-IR AO-assisted IFU spectrographs can reach much higher spectral resolutions ($R \approx 11\,000$ with VLT/ERIS), uniquely enabling a thorough study of gas kinematics via line emission, JWST's unprecedented broad wavelength coverage and high sensitivity provide imaging and spectroscopy of $z \approx 2$ galaxies across a continuous rest-frame UV to near-IR wavelength range (Ferruit et al. 2022; Rieke et al. 2023). This gives us access to a wealth of interstellar medium (ISM) and stellar population properties (e.g., metallicity, dust

⋆ Corresponding authors: eleonora.parlanti@sns.it; gtozzi@mpe.mpg.de
⋆⋆ These authors contributed equally to this work.

extinction, ionization state, and stellar mass). Moreover, with their high spatial resolution (∼0.1″), both facilities can probe physical scales down to ∼1 kpc, comparable to the Toomre scale (Toomre 1964), the fundamental scale governing gravitational instabilities in gas-rich, rotationally supported galactic disks at $z \approx 1$–3 (e.g., Genzel et al. 2011). Therefore, by leveraging both JWST and ground-based AO IFU facilities, we can now obtain a full picture of galaxies at cosmic noon, including gas kinematics, stellar properties, and ISM conditions (Park et al. 2024; Ju et al. 2025; Nestor Shachar et al. 2025; Slob et al. 2025).

In this work, we present JWST observations of K20-ID7 (GS4_29868; RA = 03:32:29.1, Dec = −27:46:28.5), a star-forming main-sequence galaxy ($M_\star \approx 4 \times 10^{10}$ M$_\odot$; Förster Schreiber et al. 2018) at $z = 2.224$, featuring a large, well-defined spiral morphology. This galaxy is an ideal laboratory for investigating many of the key mechanisms occurring at cosmic noon, from bulge growth and the settling of morphological features to star formation in kiloparsec-scale clumps and radial gas transport. Located in GOODS-South, one of the most targeted extragalactic fields, K20-ID7 has a plethora of observations from large space surveys and deep dedicated ground-based follow-ups. It was indeed extensively observed from space with the *Hubble Space Telescope* (HST) as part of the Great Observatories Origins Deep Survey (GOODS; Giavalisco et al. 2004), the Cosmic Assembly Near-Infrared Deep Extragalactic Legacy Survey (CANDELS; Grogin et al. 2011; Koekemoer et al. 2011), and the 3D-HST (Brammer et al. 2012; Skelton et al. 2014) surveys. It was also observed at longer wavelengths with *Spitzer* (Dickinson et al. 2003; Ashby et al. 2013; Whitaker et al. 2014) and *Herschel* (Lutz et al. 2011) and benefits from deep ground-based AO-assisted IFU observations at high spectral and spatial resolutions. The first deep high-resolution IFU data were obtained with VLT/SINFONI, as part of the AO SINS/zC-SINF survey (Förster Schreiber et al. 2018), where the Hα kinematics revealed a globally ordered velocity field compatible with disk rotation (Förster Schreiber et al. 2018; Espejo Salcedo et al. 2025a) and provided evidence of radial gas inflows along a spiral arm (Genzel et al. 2023). More recently, K20-ID7 was observed with VLT/ERIS at superior spectral ($R \approx 10\,500$) and spatial resolutions as part of the Guaranteed Time Observation (GTO) program GALPHYS (PI: N. M. Förster Schreiber). The detailed Hα kinematics and morphology from ERIS data have enabled a thorough study of kiloparsec-scale star-forming clumps (Förster Schreiber et al., in prep.) as well as a robust characterization of gas inflows (Pulsoni et al., in prep.).

For galaxies at $z \sim 2$, JWST data provide continuous coverage from the rest-frame near-UV to the rest-frame near-IR. K20-ID7 has a wealth of archival JWST spectroscopy and imaging, including data from the GTO JWST Deep Extragalactic Survey (JADES; Eisenstein et al. 2026) in the *Hubble* Ultra Deep Field (HUDF) and surrounding GOODS-South (Bunker et al. 2024), as well as from the Cycle 1 General Observer (GO) program First Reionization Epoch Spectroscopically Complete Observations (FRESCO; Oesch et al. 2023).

In this work, we leverage the rich dataset available for K20-ID7 to present a complete characterization of its ISM conditions and stellar properties on scales down to ∼1 kpc, thereby gaining insights into its formation and evolution mechanisms. This paper is structured as follows. In Sect. 2 we present all the data analyzed in this work from JWST, HST/ACS, and ALMA and provide details on the data reduction. In Sect. 3, we infer local ISM properties for the different galaxy regions covered by distinct MSA shutters. In Sects. 4 and 5, we focus on resolved SED fitting of NIRCam and HST imaging and discuss spatially mapping star formation via Paβ in NIRCam WFSS data. We then compare the resolved results with integrated SED analyses, including available mid- and far-IR photometry. In Sect. 6, we interpret the inferred results in the context of galaxy growth and evolution scenarios, and in Sect. 7, we draw our conclusions.

Throughout this work, we use the following notation to refer to key emission-line diagnostics:

- R2 = log([OII]$\lambda\lambda$3726,29/Hβ);
- R3 = log([OIII]λ5007/Hβ);
- O3O2 = R3 – R2;
- N2 = log([NII]λ6584/Hα);
- O3N2 = R3 – N2;
- N2O2 = log([NII]λ6584/[OII]$\lambda\lambda$3727,29);
- S2 = log[([SII]λ6716 + [SII]λ6731)/Hα];
- S23 = log[([SII]$\lambda\lambda$6716,31 + [SIII]$\lambda\lambda$9069,9533)/Hβ];
- N2S2 = log([NII]λ6584/[SII]$\lambda\lambda$6716, 31).

We adopted cosmological parameters from Planck Collaboration XIII (2016) – i.e., H_0 = 67.7 km s^{-1} Mpc^{-1}, Ω_m = 0.307, and Ω_Λ= 0.691 – and a Chabrier initial mass function (Chabrier 2003).

2. Data

In this section, we present all data employed in this paper, mostly from JWST, but also from HST (ACS images in five filters) and ALMA (Band 6 continuum at 1.2 mm), along with the data reduction. The JWST data consist of: NIRCam imaging in 11 filters; NIRSpec MSA spectra at $R \sim 100$, $R \sim 1000$, and $R \sim 2700$; and NIRCam WFSS F444W data ($R \sim 1600$).

2.1. JWST/NIRCam and HST/ACS imaging

K20-ID7 was recently observed as part of the JADES survey (Eisenstein et al. 2026) in the Hubble Ultra Deep Field (Bunker et al. 2024), which acquired NIRCam imaging in 11 different broad- and medium-band filters (F090W, F115W, F150W, F182M, F200W, F210M, F277W, F335M, F356W, F410M, and F444W), and NIRSpec MSA spectroscopy (presented in Sect. 2.2). Additional NIRCam data come from the Cycle 1 FRESCO survey (PI: P. Oesch, program ID: 1895; Oesch et al. 2023) – a NIRCam WFSS program, which obtained grism spectroscopy (see Sect. 2.3) and F444W imaging, along with parallel medium-band imaging in F182M and F210M. Among the HST imaging available, we only used publicly released HST/ACS imaging (F435W, F606W, F775W, F814W, and F850LP) from the GOODS and CANDELS surveys (Giavalisco et al. 2004; Grogin et al. 2011; Koekemoer et al. 2011) and discarded the WFC3/IR images, since they cover the same wavelengths as the bluer NIRCam filters but at a lower sensitivity and spatial resolution.

For five NIRCam filters (F182M, F210M, F277W, F356W, and F444W), we adopted the high-quality reductions publicly released on the DAWN JWST Archive[1] (DJA). These were obtained using the `grizli`[2] reduction software (Brammer 2019, 2023), which performs standard calibrations, astrometric alignment with `DrizzlePac`[3], and background subtraction optimized to preserve faint emission and minimize noise (see details in Valentino et al. 2023). Since the reduced NIRCam images in the other six filters (F090W, F115W, F150W, F200W, F335M,

[1] https://dawn-cph.github.io/dja/
[2] https://github.com/gbrammer/grizli
[3] https://www.stsci.edu/scientific-community/software/drizzlepac

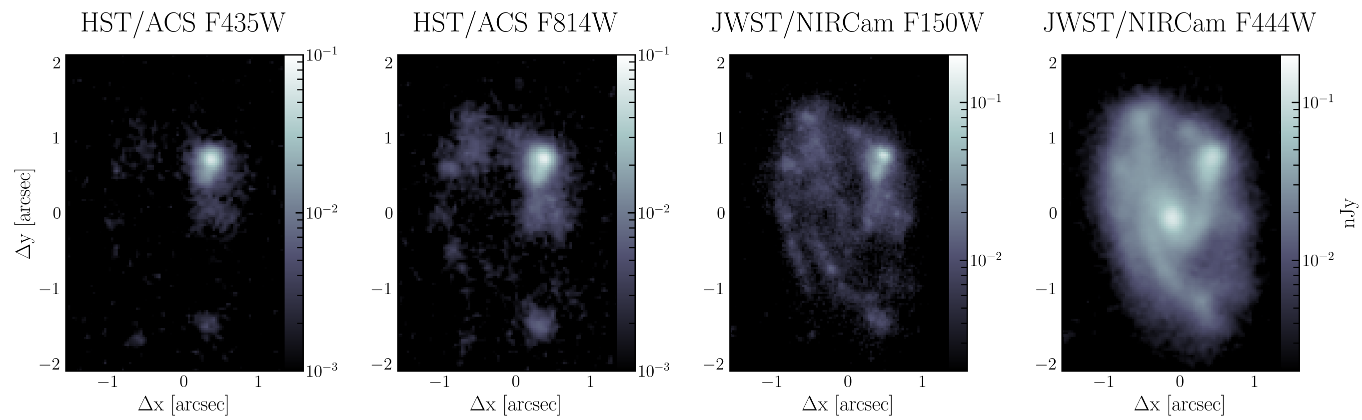

Fig. 1. Images of K20-ID7 in four representative HST/ACS (F435W, F814W) and JWST/NIRCam (F150W, F444W) filters, tracing galaxy emission from the rest-frame UV to near-IR wavelengths. Redder NIRCam imaging unambiguously reveals a regular, unperturbed galaxy morphology with well-defined spiral arms and a compact core, which is brightest in the F444W filter. All images are expressed in nanojansky.

F410M) have not yet been publicly released on DJA, we retrieved uncalibrated NIRCam data from the Mikulski Archive for Space Telescopes (MAST) portal[4], and reduced them using a custom-made reduction pipeline (see Espejo Salcedo et al. 2025b for a detailed description). This reduction leverages the CrabToolkit[5], which follows standard JWST image processing steps[6], and applies additional steps to improve the removal of artifacts through a combination of manual masking and publicly available templates (Sunnquist et al. 2025). The reduced images are then astrometrically corrected, improved with an additional flat background subtraction, and finally produced with a 0.025″ pixel scale aligned with a north up and east left orientation, consistent with DJA reductions. Similarly, we also produced HST images with the same northeast orientation and 0.025″ pixel sampling.

Figure 1 displays four representative HST/ACS (F435W and F814W) and JWST/NIRCam (F150W and F444W) images of K20-ID7, each showing the morphology of the galaxy emission at different wavelengths, from the rest-frame UV to near-IR. The comparison between JWST/NIRCam and HST/ACS images immediately highlights how crucial it is to cover redder wavelengths with JWST/NIRCam to get a complete, unambiguous view of this galaxy. At redder wavelengths, a well-defined spiral structure clearly emerges, featuring three spiral arms, bright clumps, and a compact red core that becomes particularly bright in the reddest F444W filter. A first composite-color image of K20-ID7, including the NIRCam F444W band, was presented in Genzel et al. (2023), revealing the galaxy's large outstanding spiral and the central compact core for the first time.

2.2. NIRSpec MSA spectroscopy

In addition to NIRCam imaging, the JADES survey also acquired deep NIRSpec MSA spectroscopy of targets in the HUDF and surrounding GOODS-South field at low ($R \sim 100$, with PRISM/CLEAR), medium ($R \sim 1000$, with G140M/F070LP, G235M/F170LP, and G395M/F290LP), and high resolution ($R \sim 2700$, with G395H/F290LP). In particular, K20-ID7's NIRSpec/MSA data were obtained as part of the JADES program 1210 (PI: N. Lützgendorf) and consist of two distinct datasets associated with different pointings (Fig. 2, left panel). The two pointings were centered on the two UV-bright blue clumps visible in HST/ACS imaging (see Fig. 1), which were classified as two separate entries (i.e., two distinct galaxies) in the CANDELS and 3D-HST catalogs (Skelton et al. 2014).

K20-ID7's NIRSpec/MSA data were publicly released as part of the first JADES data release (Bunker et al. 2024), along with a public reduced version of the spectra obtained using the NIRSpec MSA GTO pipeline (Scholtz et al. 2025). This pipeline applies a point-source path-loss correction and performs a local background subtraction by measuring the background in lateral shutters and subtracting it from the "science" spectrum of the central shutter. While this standard procedure has widely proven to work well for compact sources (e.g., more distant galaxies at $z > 4$; Bunker et al. 2024), it is not suitable for extended sources such as K20-ID7, where the side shutters are also placed on emitting regions of the galaxy. Therefore, if used for background measurement, they result in line and continuum emission self-subtraction. Moreover, an accurate path-loss correction is essential to properly account for both geometric losses (from galaxy light partially falling outside the micro-shutter mask) and diffraction losses (from light lost along the NIRSpec optical path). The standard pipeline performs reliable path-loss correction for either point-like sources or uniformly illuminated micro-shutters. Since K20-ID7's MSA data do not match any of these options, the standard path-loss correction in the public reduced data likely produced incorrect fluxes and altered the global spectral shape due to the wavelength dependence of the correction.

For all these reasons, we implemented a custom reduction of K20-ID7's NIRSpec/MSA spectra, which i) performs improved background subtraction and path-loss correction and ii) extracts science spectra from all MSA shutters showing galaxy emission. In the following, we describe the main steps of our adopted reduction procedure. We retrieved the count rate data from the MAST archive to extract the 2D trace of each spectrum for each visit, apply the wavelength calibration and flat-field correction, and skip the path-loss correction and background subtraction steps. After rectifying the 2D traces, we obtained 2D rectified spectra relative to each grating and filter configuration, nod, and exposure.

By visually inspecting the resulting 2D rectified spectra, we detected galaxy emission in most of the MSA shutters in the

[4] https://archive.stsci.edu/
[5] https://github.com/1054/Crab.Toolkit.JWST
[6] https://jwst-docs.stsci.edu/jwst-science-calibration-pipeline/stages-of-jwst-data-processing

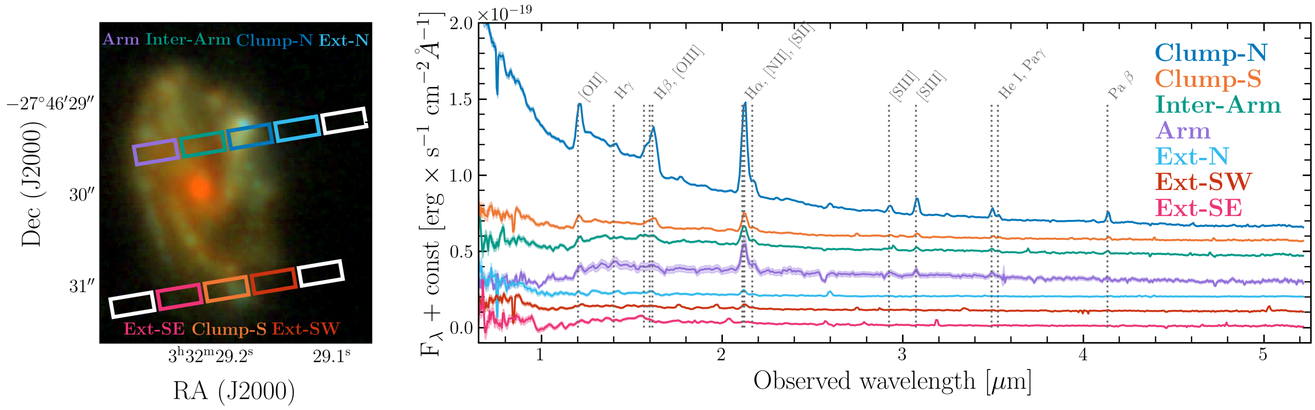

Fig. 2. NIRSpec MSA spectroscopy of K20-ID7. *Left*: Location of the two distinct MSA mask arrays, with open shutters overlaid on a NIRCam RGB image of K20-ID7 composed of F356W+F444W (red), F182M+F200W+F277W (green), and F090W+F115W+F150W (blue) filters. *Right*: PRISM/CLEAR spectra extracted from the seven colored MSA shutters (showing galaxy emission, color-coded as in the left panel), using our custom reduction pipeline (described in Sect. 2.2). The white shutters contain no galaxy emission. The spectra from different regions exhibit different continuum shapes and line intensities across the rest-frame near-UV to near-IR wavelength range. For clarity, each spectrum is vertically shifted by an arbitrary constant.

PRISM/CLEAR configuration (seven in total; the colored shutters in the right panel of Fig. 2). We therefore created a master background, which we subtracted from each shutter spectrum using the following procedure. Using the MSA pipeline, we reduced the data from all the shutters left open in the MSA mask for the same visit, focusing on specifically selected source-free regions, and created the corresponding rectified background 2D spectra. For each visit, we then generated a unique 2D master background – computed as the median of the 2D rectified background spectra – and removed it from the 2D rectified science spectra previously obtained for K20-ID7. By combining all 2D background-subtracted spectra of K20-ID7, we obtained the final 2D PRISM spectra for each visit. From these, we extracted the 1D spectra for each shutter using a 5-pixel wide slit. We also adopted the same procedure for the "error" extension of the observed data. For medium- and high-resolution data, we followed a different procedure for background subtraction, since galaxy emission is detected in fewer shutters (i.e., five) than in the PRISM/CLEAR configurations. In particular, since we do not detect galaxy emission in the light blue and pink shutters shown in the left-hand panel of Fig. 2, unlike in the PRISM data, we used these to separately measure the background for each pointing. From these two background shutters, we therefore extracted 1D background spectra using a 5-pixel-wide slit and subtracted them from the 1D science spectra extracted from the other shutters of the same visit. This yielded medium- and high-resolution spectra for four distinct regions of K20-ID7. We note that, with this approach, the expected self-subtraction effect on the Hα flux is at most ∼10%, while it is negligible for other emission lines.

Finally, to correct all MSA spectra for path losses, we measured the flux in the NIRCam images of K20-ID7 for the region encompassed by each shutter. We then used these flux values to rescale the NIRSpec/MSA spectra via a linear fit to the ratio of the observed NIRCam fluxes to the observed NIRSpec/MSA counterparts in each shutter.

In summary, with our custom MSA reduction, we obtain in total seven PRISM/CLEAR spectra (see Fig. 2) and five spectra for each medium- and high-resolution grating and filter configuration. All together these spectra probe seven distinct galaxy regions: clumps (labeled as Clump-N and Clump-S), spiral arm (Arm), inter-arm (Inter-Arm), and more external diffuse regions (Ext-N, Ext-SW, and Ext-SE). Both low-resolution PRISM ($R \sim 100$) and all medium-resolution spectra ($R \sim 1000$) cover a total spectral range from 0.6 μm to 5.2 μm, corresponding to rest-frame near-UV to near-IR wavelengths at $z \sim 2$. In contrast, high-resolution observations ($R \sim 2700$) were only obtained with the reddest grating (i.e., G395H/F290LP) and are, therefore, limited to the 2.9–5.2 μm wavelength range encompassing K20-ID7's rest-frame near-IR emission. Details on the covered wavelength range, spectral resolution, and exposure time relative to each MSA grating and filter configuration are summarized in Table 1. The exposure time reported refers to the central shutter of each array; the exposure time decreases to 2/3 and 1/3 with increasing distance from the central shutter.

Table 1. NIRSpec/MSA observations of K20-ID7 used in this paper.

Dataset	$\Delta\lambda$ [μm]	R	t_{exp} [ks]
PRISM/CLEAR	0.6–5.3	30–300	33.6
G140M/F070LP	0.7–1.9$^{(\star)}$	500–890	8.4
G235M/F170LP	1.7–3.2	720–1340	8.4
G395M/F290LP	2.9–5.2	730–1315	8.4
G395H/F290LP	2.9–5.2	1930–3615	8.4

Notes. The columns list the wavelength coverage, nominal spectral resolution (Ferruit et al. 2022), and exposure time of the observations in each distinct grating and filter comnfigurations. The t_{exp} values reported here refer to the central shutter for each visit. $^{(\star)}$The nominal wavelength range is 0.7–1.3 μm. However, as in JADES (Bunker et al. 2023), we recover the spectrum up to 1.9 μm, effectively acting as G140M/F070LP+F100LP.

2.3. NIRCam WFSS data

In this work, we used JWST/NIRCam WFSS F444W observations of K20-ID7 from FRESCO (Oesch et al. 2023), obtained with an exposure time of 7 ks. These consist of grism spectra covering the range 3.8–5.0 μm at a spectral resolution of

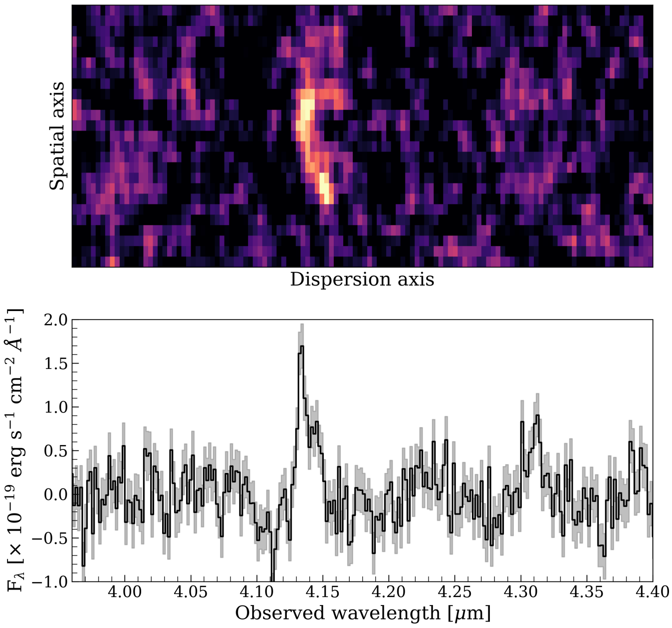

Fig. 3. Continuum-subtracted NIRCam F444W WFSS data of K20-ID7, zoomed-in over 3.95–4.40 µm, encompassing Paβ line emission. In the 2D slitless spectra (upper panel), the Paβ line emission is clearly spatially resolved perpendicular to the dispersion axis and extended along the parallel direction. This results in a double-peaked Paβ line profile in the total 1D spectrum (lower panel), a consequence of resolved spatial offsets combined with velocity gradients along the grism dispersion axis (discussed in Sect. 5).

$R \sim 1600$, which probe rest-frame near-IR wavelengths at $z \sim 2$. Slitless spectra of K20-ID7 were acquired with the grism dispersion axis at a 90° position angle (i.e., aligned WE, with increasing wavelengths toward E). All FRESCO NIRCam WFSS data, including those of K20-ID7, were reduced using the publicly available `grizli` code (Brammer et al. 2012; Brammer 2023). Continuum-subtracted spectra were then produced by running a median filter along each row of the 2D grism spectra, adopting a 12-pixel central gap in the filtering to minimize line self-subtraction (Kashino et al. 2023). For further details on the observational design and reduction of FRESCO observations, we refer the reader to the main papers of the survey (e.g., Oesch et al. 2023; Nelson et al. 2024; Neufeld et al. 2024).

As shown in Fig. 3, the continuum-subtracted spectra of K20-ID7 clearly exhibit Paβ line emission. The Paβ line is detected with a total S/N of 7, computed as the ratio between the integrated line flux and the noise level estimated from the error spectrum. We derived the total flux by fitting the spectrum with a model consisting of a linear continuum and two Gaussian components. The error was estimated using two Gaussian components with the same line widths and amplitudes equal to the error level. No additional emission lines are detected. Compared to optical Balmer emission lines (e.g., Hα and Hβ), near-IR Paschen lines are less affected by dust attenuation and, therefore, can probe recent (∼10 Myr) star formation in a more obscured regime. In the 2D slitless spectra (upper panel), Paβ appears spatially resolved along the spatial axis (i.e., perpendicular to the grism dispersion axis) and extended along the spectral axis. This results in a double-peaked Paβ line profile in the total 1D spectrum (lower panel). As later addressed in Sect. 5, this is a consequence of real spatial offsets combined with velocity gradients along the grism dispersion axis.

2.4. ALMA data

We reduce the available ALMA Band 6 1.2 mm continuum data (PI: J. Scholtz, program ID 2018.1.01044.S) using `CASA`. We retrieve the raw visibilities from the ALMA archive, and calibrate them by executing the script delivered with the data. We then clean the data by using the task `tclean` in `CASA`, and image them using natural weighting and a pixel scale of 0.1″ to obtain the best sensitivity. The final continuum image has an angular resolution of 0.5″ ×0 .6″ and a sensitivity of 28 µJy beam^{-1}. We compute the continuum flux by summing all pixels within a circular aperture of radius 2″. The uncertainty on the observed flux is estimated via a Monte Carlo approach: we randomly placed 5000 apertures of the same size in regions free of galaxy emission and measured the flux in each, hence we assumed as an error the standard deviation of the resulting distribution. Following this analysis we obtain a 1.2 mm continuum flux of 0.36 ± 0.11 mJy.

3. Local ISM properties from spectroscopy

The wavelength range covered by the NIRSpec MSA data (∼0.7–5.2 µm) encompasses several emission lines, which we used to infer the properties of the galactic ISM via various emission-line diagnostics. In particular, we derived nebular dust attenuation, the ionization parameter, electron density ($A_{V,\mathrm{neb}}$, $\log(U)$, n_e), and chemical abundances (O, N, S) for the galaxy regions where the key emission lines are detected at S/N > 3. In Appendix A, we describe the spectral fitting of the MSA spectra and summarize the best-fit results. For shutters where the same emission lines were detected with more than one spectral setup, we adopted the line fluxes from the medium-resolution data as fiducial. These have a higher S/N than the high-resolution data and resolve close spaced emission lines (e.g., Hβ+ [OIII], Hα + [NII], [SII] line doublet) well, unlike the PRISM data. Therefore, when available, we only used the medium-resolution line fluxes to derive ISM properties, thereby also avoiding issues related to possible inaccuracies in the absolute flux calibration (D'Eugenio et al. 2025).

3.1. Dust attenuation, ionization, and electron density

The first important physical property to derive is the (nebular) dust attenuation ($A_{V,\mathrm{neb}}$), which allows us to correct all observed line fluxes and then measure the other ISM properties. Within the broad spectral range covered by the NIRSpec MSA data of K20-ID7, there are several hydrogen emission lines (i.e., Hδ, Hγ, Hβ, Hα, Paγ, Paβ), which can be used to infer multiple measurements of $A_{V,\mathrm{neb}}$ from distinct line ratios. In Table 2, we report our derived $A_{V,\mathrm{neb}}$ measurements, obtained by combining the highest S/N hydrogen lines (i.e., Hβ, Hα, Paβ, when detected). We assumed the Calzetti et al. (2000) dust attenuation law and adopted theoretical line ratios of 2.86, 0.0569, 0.163 – as predicted for warm ionized gas (T = 10^4 K; Osterbrock & Ferland 2006) – for Hα/Hβ, Paβ/Hα, and Paβ/Hβ, respectively. For the inter-arm region, we derived $A_{V,\mathrm{neb}}$ from the Paβ/Hα ratio only, since no measurements for the Hβ flux are available in this shutter[7]. For the clump regions (Clump-N and Clump-S), where all three hydrogen lines are detected, we obtain consistent measurements of $A_{V,\mathrm{neb}}$ from different hydrogen line ratios within 2σ.

[7] For the inter-arm region, Hβ is only detected in the PRISM spectrum but appears blended with [OII]$\lambda\lambda$5007,4959. Therefore, it cannot be disentangled.

Table 2. ISM properties inferred from NIRSpec MSA spectra for the three higher-S/N shutters of K20-ID7.

Diagnostic	Arm	Inter-Arm	Clump-N	Clump-S
		$A_{V,\mathrm{neb}}$ [mag]		
Hα/Hβ	–	–	$0.6^{+0.1}_{-0.1}$	<0.9
Paβ/Hα	–	$1.3^{+0.4}_{-0.5}$	$0.2^{+0.1}_{-0.1}$	$0.6^{+0.4}_{-0.6}$
Paβ/Hβ	–	–	$0.4^{+0.1}_{-0.1}$	$0.3^{+0.3}_{-0.4}$
Fiducial	–	$1.3^{+0.4}_{-0.5}$	$0.4^{+0.1}_{-0.1}$	$0.4^{+0.3}_{-0.3}$
		n_e [cm^{-3}]		
[SII]	–	<1900	260^{+120}_{-139}	<310
		log(U)		
[SII], [SIII]	–	$-3.3^{+0.3}_{-0.2}$	−3.05 ± 0.05	−3.0 ± 0.2
[OII], [OIII]	–	$-3.1^{+0.3}_{-0.5}$	−2.97 ± 0.02	−3.1 ± 0.1
Fiducial	–	−3.3 ± 0.3	−3.01 ± 0.03	−3.1 ± 0.2
		12+log(O/H)		
Fiducial	$8.57^{+0.20}_{-0.21}$	$8.58^{+0.06}_{-0.06}$	$8.49^{+0.06}_{-0.06}$	$8.51^{+0.08}_{-0.08}$
		log(N/O)		
N2O2	–	−0.8 ± 0.2	−0.95 ± 0.05	−1.1 ± 0.1
N2S2	–	−0.9 ± 0.2	−0.95 ± 0.10	−1.2 ± 0.2
Fiducial	–	−0.9 ± 0.2	−0.95 ± 0.08	−1.2 ± 0.2
		12+log(S/H)		
S23	–	$6.6^{+0.2}_{-0.2}$	$6.6^{+0.2}_{-0.2}$	$6.7^{+0.3}_{-0.2}$
		log(S/O)		
	–	−2.0 ± 0.2	−1.9 ± 0.2	−1.8 ± 0.3

Notes. Top to bottom: Nebular attenuation $A_{V,\mathrm{neb}}$, derived from different hydrogen line ratios (Calzetti et al. 2000); electron density n_e derived from the [SII] line ratio (Sanders et al. 2016); ionization parameter log(U) using sulfur- and oxygen based diagnostics (Díaz et al. 2000); gas-phase metallicity (12+log(O/H)) derived by combining various strong-line diagnostics (Sanders et al. 2025); log(N/O) abundance (Hayden-Pawson et al. 2022); 12+log(S/H) abundance (Díaz & Zamora 2022); log(S/O) abundance, derived by combining the 12+log(S/H) and the fiducial 12+log(O/H) values. All upper limits correspond to 2σ.

Small differences in the derived A_V values using different line ratios may be due to the different shapes of attenuation curves at high redshift (Markov et al. 2025) compared to local ones. To verify this, we also computed $A_{V,\mathrm{neb}}$ by adopting the high-z attenuation curve by Reddy et al. 2026, finding values comparable within the uncertainty with our estimates reported in Table 2. In the rest of this section, we adopt as fiducial values the weighted averages of the available measurements for each region, as reported in Table 2[8]. For the Arm region, Hα is the only hydrogen line detected, so we cannot estimate $A_{V,\mathrm{neb}}$. However, this is not crucial, since [NII] and Hα are the only emission lines detected in this region. Thus, we can only use the [NII]/Hα emission-line diagnostic (discussed in Sect. 3.3 to derive metallicity), for which dust extinction is negligible due to the proximity of these lines in wavelength. We reiterate that the $A_{V,\mathrm{neb}}$ values inferred in this section from hydrogen line ratios refer to nebular dust attenuation, which might be higher than the attenuation affecting stellar continuum ($A_{V,\mathrm{star}}$ inferred from SED modeling in Sect. 4), since HII regions are typically more embedded in dust.

Following Sanders et al. (2016), we then measured n_e from the dust-corrected [SII]λλ6716, 31 line doublet. For Clump-N, we find an electron density of $n_e \simeq 260\,\mathrm{cm}^{-3}$, consistent with the typical values inferred for $z \approx 2$ star-forming regions (Sanders et al. 2016; Davies et al. 2021; Topping et al. 2025). Unfortunately, the [SII]λ6717/λ6731 ratio for the other two regions (i.e., Clump-S and Inter-Arm) yields nonphysical (negative) values of n_e; therefore, we adopted a conservative 2σ upper limit.

Given the high sensitivity and the wide wavelength coverage of K20-ID7's NIRSpec/MSA spectra, we derived two independent measurements of the ionization parameter from the [OII] /[OIII] and [SII]/[SIII] line ratios, respectively, for each high-S/N galaxy region. The [SIII]λ9069 emission line is detected in the medium-resolution grating only in the Clump-N spectra. However, we can estimate it for the inter-arm and Clump-S regions using the dust-corrected flux of the [SIII]λ9533 line, assuming a theoretical ratio of [SIII]λ9533/[SIII]λ9069 = 2.61 (Osterbrock & Ferland 2006). We note that for Clump-S, we have a measurement of the [SIII]λ9069 from the PRISM spectrum. However, most of the PRISM data are affected by a bad feature near this emission line (see Fig. A.1). Finally, we obtain a dust-corrected flux of [SIII]λ9069 of $\sim 2.7 \times 10^{-19}$ erg s^{-1} cm^{-2} and 3.2×10^{-19} erg s^{-1} for the inter-arm and Clump-S regions, respectively. Using the [OII]/[OIII]- and [SII]/[SIII]-based calibrators from Díaz et al. 2000, we thus infer two independent values of log(U) for each region. All inferred measurements indicate log(U) ≃ − 3.0 for both Clump-N and Clump-S, with a similar value – albeit with larger uncertainties – for the inter-arm region. This value is low, yet consistent with findings for other high-z galaxies (Reddy et al. 2023a).

3.2. Gas phase metallicity

In this work, we used metallicity calibrations from Sanders et al. (2025), based on six distinct diagnostics, namely R2, R3, O32, N2, O3N2, and S2 (see the end of Sect. 1 for all definitions). For the inter-arm region, where direct flux measurement of the Hβ emission lines needed for four diagnostics were unavailable, we estimated the Hβ flux from our fiducial dust-extinction-corrected Hα flux (i.e., measured from medium-resolution data and corrected for $A_{V,\mathrm{neb}} = 1.3^{+0.4}_{-0.5}$; see Table 2). We assumed a theoretical Hα/Hβ line ratio of 2.86 (Osterbrock & Ferland 2006), yielding an Hβ flux of 2.75×10^{-17} erg s^{-1} cm^{-2} for the inter-arm region. In the Arm region, we only used N2, since Hα and [NII] are the only detected emission lines.

Following an approach similar to that described in Curti et al. 2020a, we derived the metallicity that simultaneously minimizes the χ^2 between the observed line ratios and the expected value according to each calibrator using the `python` library `lmfit`. The resulting best-fit metallicity values, including their errors (which account for the intrinsic scatter of the calibrators), are reported in Table 2. We find no statistically significant difference in metallicity between the various regions. The values are consistent within the uncertainties and indicate slightly subsolar metallicities, with 12 + log(O/H) = 8.49–8.58 (i.e., ∼0.60–0.80 $Z_\odot$[9]). Nonetheless, it is interesting that the star-forming clumps, where newborn stars are expected to inject metals into the ISM, do not exhibit higher metallicity than the other regions. We speculate that any more prominent intrinsic differences (if present) may be smoothed out by the spatial

[8] For Clump-S, we consider only the two inferred $A_{V,\mathrm{neb}}$ estimates, excluding the upper limit derived from Hα/Hβ.

[9] We assumed a solar metallicity 12 + log(O/H)$_\odot$ = 8.69 (Asplund et al. 2021).

extent of the shutters, which encompass emission from physically distinct regions. Indeed, the Clump-N shutter is not perfectly centered on the clump, and the Inter-Arm shutter may be contaminated by emission from the clump close by (see Fig. 2). Interestingly, all the derived metallicities are consistent with that expected from the fundamental metallicity relation (FMR; Mannucci et al. 2010) for K20-ID7, given its stellar mass and SFR ($M_\star \approx 4\times10^{10}\,M_\odot$ and $SFR \approx 120\,M_\odot\,yr^{-1}$, inferred later in Sects. 4 and 5). Using the parameterization by Curti et al. (2020b), the FMR predicts a gas-phase metallicity of $12+\log(O/H)\approx 8.57$. As discussed in Sect. 6.2, this is connected to the presence of gas inflows (Genzel et al. 2023; Pulsoni et al., in prep.).

3.3. Chemical abundances: N/O, S/H, S/O

Among chemical elements, nitrogen is one of the most extensively studied, from the local Universe up to high redshifts (Pilyugin et al. 2012; Shapley et al. 2015; Masters et al. 2016; Strom et al. 2018; Stiavelli et al. 2025; Sanders et al. 2025). In star-forming galaxies, its abundance can be derived from the relatively bright [NII] and [OII] emission lines, via the N2O2 diagnostic (e.g., Steidel et al. 2016; Strom et al. 2018; Hayden-Pawson et al. 2022). Since these lines originate from nearly the same ionization zones and have similar ionization potentials, their ratio minimally depends on ISM ionization conditions. Alternatively, one can infer N/O using the N2S2 diagnostic, which assumes a constant S/O abundance. This method is less affected by dust extinction, since the lines involved are closer in wavelength than [NII] and [OII] in N2O2. Yet, the [SII] emission lines have a lower ionization potential (10.4 eV) and, therefore, may be emitted from regions with softer radiation fields. Moreover, the assumption of a constant S/O abundance, which is necessary to use [SII] as a proxy for oxygen, may not always be true. For all these reasons, we provide two independent measurements of N/O in the various galaxy regions, adopting the calibrations from Hayden-Pawson et al. (2022) (see Table 2). For each region, N2O2- and N2S2 diagnostics deliver consistent, values-based N/O ratios. We adopted their average as the fiducial value. The N/O abundance in Clump-S is 0.3 dex higher than in the Inter-Arm, with the Clump-N lying between the two. We obtain similar results by also using the calibrations for N2O2 and N2S2 presented in Strom et al. (2018).

Similar to oxygen, sulfur is produced by massive stars; therefore, the relative S/O abundance is expected to remain constant at about the solar value (i.e., $\log(S/O)_\odot = -1.57$; Asplund et al. 2021). A sulfur abundance of $12+\log(S/H)$ has been studied only for a handful of galaxies at $z>1$ (e.g. Sanders et al. 2020; Rogers et al. 2024, 2026) and can be derived from the optical [SII] and [SIII] emission lines. Compared to the [OII] and [OIII] lines used to infer $12+\log(O/H)$, the sulfur lines have a milder (albeit exponential) dependence on electron temperature, due to their lower ionization potential, which makes them detectable even at solar or supersolar abundances (Díaz et al. 2007). For K20-ID7, we estimated $12+\log(S/H)$ from the S23 diagnostic (Díaz & Zamora 2022; see Table 2). Interestingly, all three examined galaxy regions consistently feature a subsolar S/H abundance ($12+\log(S/H)_\odot = 7.12$; Asplund et al. 2009), that is $12+\log(S/H)\approx 6.6-6.8$. By finally combining these measurements of $12+\log(S/H)$ with our derived fiducial values of $12+\log(O/H)$, we estimate a relative log(S/O) abundance of about -1.9, consistent for all regions, which is systematically lower than the expected nearly constant (solar) value of -1.57 ± 0.05 (Asplund et al. 2021). In Sect. 6.3, we investigate the implications of this result, discussing possible formation and depletion channels for sulfur.

4. Resolved SED fitting

In this section, we present a spatially resolved SED model of high-resolution JWST/NIRCam and HST/ACS imaging to derive 2D maps of the main galaxy's physical properties (e.g., stellar mass, age, dust attenuation, and SFR). We then compare the resolved results with those obtained from integrated SED fitting, which includes low-resolution photometry at longer wavelengths, as well as those inferred from NIRSpec MSA in Sect. 3.

4.1. PSF matching and SED modeling with CIGALE

We matched all reduced $6'' \times 6''$ cutouts to the spatial resolution of the F444W band (FWHM = 0.15″). For JWST/NIRCam and HST/ACS data, we used `WebbPSF` models and empirical PSFs from 3DHST (Skelton et al. 2014) to create F444W matching kernels using the `python` package `photutils.psf.matching` and thus convolved each image to the F444W PSF. To estimate the background noise to adopt as the error on pixel fluxes while accounting for spatial correlations between pixels introduced by the data reduction, PSF matching, and instrumental features, we created a segmentation map for each cutout and performed flux measurements in 100 randomly placed "empty" apertures. These measurements were taken for a suite of aperture sizes with variable linear sizes of N pixels (up to $N=10$; see also Tacchella et al. 2015b). We derived the effective rms from the flux distribution as a function of aperture size and quantified the rms within one pixel. Since the effective rms is expected to be spatially constant at a fixed aperture size, we associated this error with the flux of all pixels in a given cutout. An additional contribution comes from Poisson noise, which might be significant in bright regions. From the reduced HST and JWST images of K20-ID7 (in counts), we find that Poisson noise varies across the galaxy and with spectral band, ranging from negligible to 30%–60% above the background noise. This translates to relative Poisson uncertainties in pixel flux from approximately 0.1% to a few percent. To account for this additional variable noise contribution, we conservatively included an additional 10% error on all pixel fluxes in our SED model.

To model the SED of individual pixels, we used the SED fitting code `CIGALE` (Boquien et al. 2019) and only fit the SED of pixels with $S/N>7$ on the F444W band, based on the noise estimate inferred above. This adopted S/N threshold enables continuous mapping of the whole galaxy and guarantees a $S/N \gtrsim 2$ in the bluer NIRCam filters, which indeed yields good reduced χ^2 values ($\chi^2_{red}\approx 1$) in individual pixel fits (see Fig. 4, bottom right panel). The SED of each $S/N(F444W)>7$ pixel was then modeled independently from the other pixels under the same set of assumptions. For all pixels, we fixed the redshift to $z=2.224$, as measured from Hα (Förster Schreiber et al. 2018), and assumed a decaying exponential star formation history (SFH). We allowed ages since the onset of star formation to range from 50 Myr and 2900 Myr (i.e., the age of the Universe at $z=2.224$), with e-folding timescales τ spanning 10 Myr to 8000 Myr (i.e., approximately corresponding to a constant SFH). We adopted the Bruzual & Charlot (2003) stellar population synthesis models, assuming a Chabrier (2003) initial mass function, and fixing the metallicity to $Z=0.008$[10], to reduce the number of free param-

[10] `CIGALE` only provides limited metallicity values (i.e., $Z=0.008$ and $Z=0.02$), with no intermediate value in between.

eters and avoid degeneracy with other physical quantities. This metallicity value (corresponding to $0.4\,Z_\odot$) is slightly lower than that inferred in Sect. 3.2. Yet, we find it delivers better results compared to fixing the metallicity to the solar value ($Z = 0.02$). In addition, we assumed the Calzetti et al. (2000) attenuation law and included nebular emission. We adopted suitable priors consistent with the ISM properties inferred in Sect. 3, while allowing a sufficiently large parameter space to also reproduce the properties of regions across the full system, including those that may differ from the regions for which we have measurements from the MSA spectra. Among these, we set a two-value grid for n_e ($100\,\mathrm{cm}^{-3}$ and $1000\,\mathrm{cm}^{-3}$) and allowed $\log(U)$ to vary from -3.4 and -2.0. With all these ingredients, our resolved SED model reproduces the variety of single-pixel SED shapes well, which reflect the different intrinsic natures and properties of distinct galaxy regions, such as clumps, spiral-arm regions, and inter-arm regions (see Appendix B for representative examples of best-fit SEDs).

4.2. 2D maps of host galaxy properties

Figure 4 displays the resulting spatially resolved maps of relevant galaxy parameters, computed in CIGALE as the likelihood-weighted mean of the following priors: stellar mass ($M_\star$), average SFRs computed over the last 10 Myr and 100 Myr (SFR10 and SFR100, respectively); stellar dust attenuation ($A_{V,\mathrm{star}}$); stellar age (t_age); and reduced χ^2. Table 3 summarizes the main physical properties for the most relevant regions (i.e., bulge and clumps), extracted using dedicated apertures (Fig. 5), and for the whole galaxy. In particular, for the central red compact core, we adopted a $0.25''$-diameter aperture, corresponding to twice its effective radius. This was measured by modeling the F444W image with GALFIT (Peng et al. 2002), using a double Sérsic profile (Caon et al. 1993) (Pulsoni et al., in prep.). One of the two components was used to reproduce the extended disk (Sérsic index $n_\mathrm{disk} = 0.35 \pm 0.01$, $R_\mathrm{e,disk} = 6.5 \pm 0.2$ kpc), while the other was used to reproduce the central mass concentration ($n_\mathrm{core} = 1.16 \pm 0.06$, $R_\mathrm{e,core} = 1.01 \pm 0.14$ kpc). With $n_\mathrm{core} = 1.16 \pm 0.06$, the central core is best classified as either a disky- or pseudo-bulge (Kormendy & Kennicutt 2004; detailed discussion will be presented in Pulsoni et al., in prep.). In the remainder of the paper, we simply refer to this central component as "bulge", with no attempt to interpret its dynamical nature, which is beyond the purpose of this paper.

The most prominent feature in the stellar mass map is the central bulge ($M_{\star,\mathrm{Bulge}} = (7 \pm 3) \times 10^9\ \mathrm{M}_\odot$), which is then followed by the brightest and largest star-forming clump, Clump A ($M_{\star,\mathrm{A}} = (3.5 \pm 0.7) \times 10^9\,\mathrm{M}_\odot$). With a total galaxy stellar mass of ($M_\star = (3.7 \pm 1.0) \times 10^{10}\ \mathrm{M}_\odot$), we find that the bulge and Clump A contribute by 19% and 9%, respectively. The SFR10 map follows the clumps and the spiral arms well, whose locations are visually highlighted by the dashed contours and reveal recent active star formation in the central bulge ($\mathrm{SFR10_{Bulge}} = 12 \pm 8\,\mathrm{M}_\odot\ \mathrm{yr}^{-1}$). Averaged over a longer time frame, the SFR100 map displays a different morphology: Clump A has been forming stars intensely for the last 100 Myr, while Clump-B and the spiral arms show weaker past activity than the bulge and Clump A, except for the spiral arm region between them. Interestingly, the bulge and its surroundings appear to have experienced enhanced star formation over the last 100 Myr ($\mathrm{SFR100_{Bulge}} = 82 \pm 42\,\mathrm{M}_\odot\,\mathrm{yr}^{-1}$), suggesting that the bulge formed its stars mostly in the past.

In terms of dust extinction, the stellar attenuation map ($A_{V,\mathrm{star}}$) indicates the highly obscured nature of the nuclear region ($A_{V,\mathrm{star}} = 2.83 \pm 0.24$). If we account for extra nebular line emission attenuation (i.e., $A_{V,\mathrm{neb}} \approx A_{V,\mathrm{star}}/0.44$; Calzetti et al. 2000), we obtain $A_{V,\mathrm{neb}} = 6.43 \pm 0.55$. Significant extinction ($A_{V,\mathrm{star}} = 1.5 \simeq 2.0$) is also found in regions of intense star formation, such as along the spiral arms, in Clump B, and around Clump A. The core of Clump A, in contrast, appears less attenuated ($A_{V,\mathrm{star}} \simeq 0.5$), consistent with the fact that it is also detected in the rest-frame UV.

Finally, the stellar age map suggests a trend toward the inner galaxy regions: younger stars ($t_\mathrm{age} = 50$–100 Myr) preferentially lie in the clumps, while older populations dominate the bulge and the inter-arm regions ($t_\mathrm{age} \approx 400$–$2000$ Myr). The relatively old ages inferred for the bulge, combined with its elevated SFR100, furthermore indicate that it formed most of its stellar mass in the past, while continuing to maintain low star formation activity. However, stellar age is more uncertain than the other inferred parameters, with typical uncertainties of 50%–70% on single pixels.

An alternative scenario could involve an unattenuated, quiescent bulge with extremely old stars and no recent star formation, which would still explain its observed red color. To test this hypothesis, we extracted the bulgeś integrated SED using our adopted $0.25''$ aperture and fit it with CIGALE, following the same prescriptions as in Sect. 4.1 but with $A_{V,\mathrm{star}} = 0$. With this assumption, we obtain a poor best-fit ($\chi^2_\mathrm{red} = 12$), as the model fails to reproduce the observed SED at redder wavelengths. The observed slope is much steeper than the best-fit $A_{V,\mathrm{star}} = 0$ model, which flattens and does not reproduce most of the NIRCam photometry.

In Appendix D, we validate the results from our resolved SED fitting, by comparing the 2D Hα distribution inferred from the dust corrected SFR with the observed Hα flux observed with ERIS. Figure D.1 show that the Hα flux expected from the SED fitting is overall in good agreement with the observed ERIS Hα line map at similar angular resolutions (Pulsoni et al., in prep.).

4.3. Integrated SED fitting

In this section, we discuss our SED modeling of integrated HST/ACS and JWST/NIRCam photometry, using the same assumptions as in Sect. 4.1, to compare the resolved and integrated results. To extract the total HST and JWST photometry from the reduced cutouts, we summed the flux contained in all pixels within the S/N(F444W) > 7 region defined in Sect. 4.1 and estimated the corresponding error by summing pixel uncertainties in quadrature. Results from this integrated SED fitting, including up to NIRCam F444W photometry, are summarized in Table 3 (see the column labeled $\mathrm{Galaxy_{4.4\mu m}}$; the best-fit model is shown in Appendix B).

Among all physical parameters, $M_\star$ is the most robustly constrained based on the available rest-frame optical HST/ACS and near-IR JWST/NIRCam photometry, whereas the other quantities would require coverage at longer mid- and far-IR wavelengths to constrain dust emission. As reported in Sect. 4.2, the total stellar mass of K20-ID7, computed as a sum of all pixels, is $M_\star = (3.7 \pm 1.1) \times 10^{10}\ \mathrm{M}_\odot$. This total value is slightly higher than the integrated result ($M_\star = (2.3 \pm 0.5) \times 10^{10}\ \mathrm{M}_\odot$) by about a factor of 1.6, yet the two agree within the uncertainties. This difference likely reflects outshining effects from a young stellar population, which lead to underestimated mass-to-light ratios in integrated SED modeling (e.g., Maraston et al. 2010; Wuyts et al. 2012; Giménez-Arteaga et al. 2023). Previous studies (e.g., Sorba & Sawicki 2018; Giménez-Arteaga et al. 2023, 2024) indicate that stellar masses can indeed be underestimated

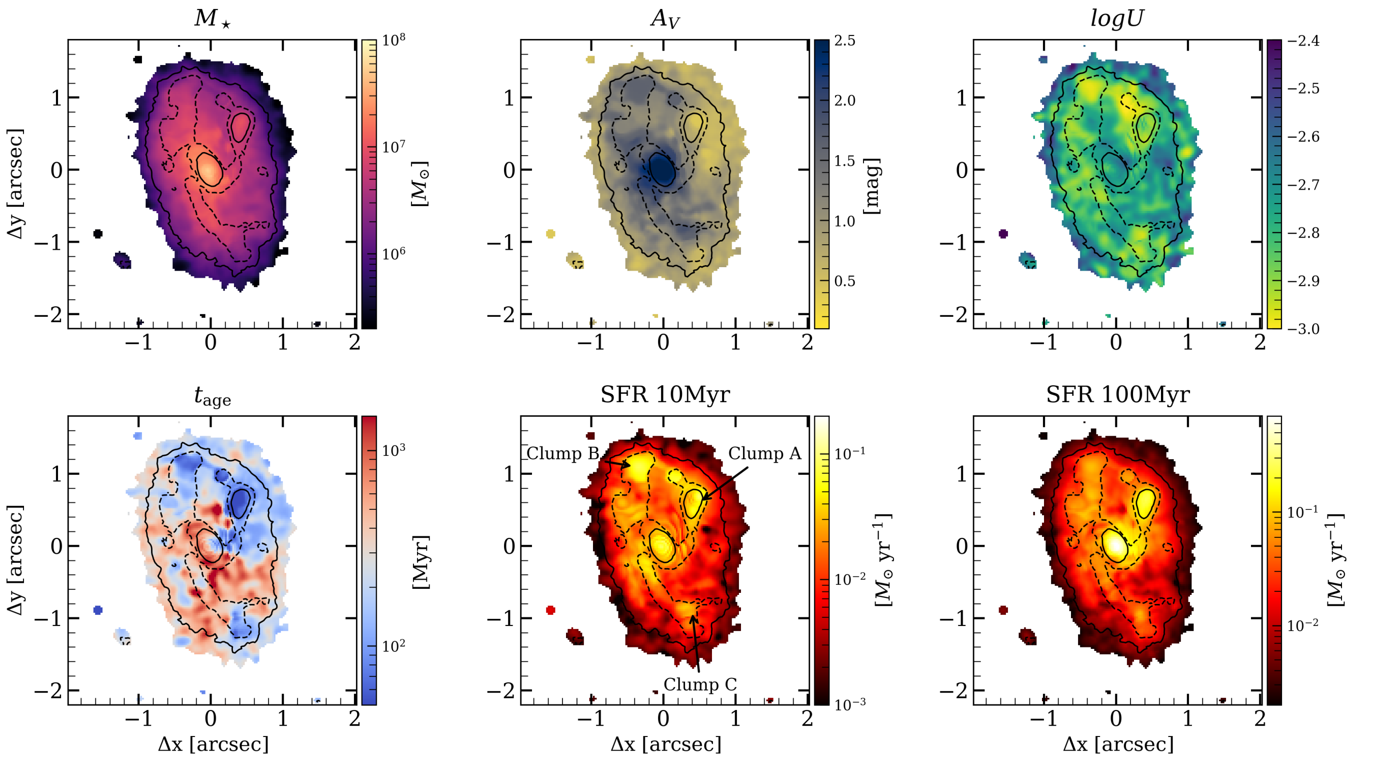

Fig. 4. 2D maps at a 25 mas pixel scale of the main galaxy properties derived from our resolved SED fitting with CIGALE of HST/ACS and JWST/NIRCam images. *Left to right*, top: Maps of stellar mass and SFRs averaged over the last 10 Myr and 100 Myr. *Bottom*: A_V, star, stellar age, and $\chi^2_{\rm red}$. The $\chi^2_{\rm red}$ map shows the goodness of our pixel-by-pixel SED model, with values ~1 across the entire galaxy. The solid contours correspond to 10 and 100σ levels of F444W continuum emission, highlighting the locations of the bright Clump A and of the bulge. The dashed lines trace the spiral arms and represent the 3σ contours of the residual F444W emission, obtained by subtracting the F444W image from a Gaussian-smoothed version with a kernel of 10 pixels. The location of the three main star-forming clumps is highlighted in the SFR10 map.

Table 3. Physical properties of the bulge, clumps, and whole galaxy, derived from our SED fitting and analysis of the Paβ line emission.

	Resolved					Integrated	
	Bulge	Clump A	Clump B	Clump C	Galaxy	Galaxy$_{4.4\,\mu m}$	Galaxy$_{1.2mm}$
d [″]	0.25	0.8	0.5	0.3	3	3	3
$M_\star$ [10^9 M$_\odot$]	7 ± 3 $^{(\star)}$	3.5 ± 0.7	1.5 ± 0.3	0.67 ± 0.19	37 ± 10	23 ± 5	36 ± 8
$t_{\rm age}$ [Myr]	<850	123 ± 75	136 ± 103	<483	288 ± 178	<223	413 ± 294
$A_{V,\rm star}$ [mag]	2.83 ± 0.24	0.77 ± 0.11	1.50 ± 0.16	1.58 ± 0.21	1.01 ± 0.22	1.19 ± 0.07	1.01 ± 0.09
SFR10 [M$_\odot$ yr^{-1}]	12 ± 8 $^{(\star)}$	21 ± 6	13 ± 4	2.8 ± 1.3	109 ± 66	93 ± 20	71 ± 19
SFR100 [M$_\odot$ yr^{-1}]	82 ± 42 $^{(\star)}$	54 ± 17	18 ± 6	6 ± 3	288 ± 178	384 ± 143	146 ± 130
SFR$_{\rm UV+IR}$ [M$_\odot$ yr^{-1}]	–	–	–	–	–	–	105 ± 17
SFR$^0_{\rm Pa\beta}$ [M$_\odot$ yr^{-1}]	1.2 ± 1.0$^{(\star)}$	21 ± 5	10 ± 2	3 ± 1	–	66 ± 22	
SFR$_{\rm Pa\beta}$ [M$_\odot$ yr^{-1}]	$7.6^{+8.8}_{-6.6}$ $^{(\star)}$	24^{+6}_{-7}	11^{+2}_{-2}	$3.4^{+1.6}_{-1.0}$	–	120^{+70}_{-70}	
$A_{V,\rm neb}$	6.43 ± 0.55	$0.4^{+0.1}_{-0.1}$	$0.4^{+0.1}_{-0.1}$	$0.4^{+0.3}_{-0.3}$	–	2.0 ± 0.6	

Notes. For the galaxy, we provide SED-based results from resolved maps (Galaxy) and integrated models, including photometry up to 4.4 µm (Galaxy$_{4.4\mu m}$) and 1.2 mm (Galaxy$_{1.2mm}$). From top to bottom, we list: the diameter (d) of the apertures (shown in Fig. 5) used to sum or average pixel values in resolved maps, and for the integrated analysis; the SED-based physical parameters (Sect. 4), i.e., stellar mass ($M_\star$), age ($t_{\rm age}$), and stellar dust attenuation ($A_{V,\rm star}$); SFRs averaged over the last 10 Myr and 100 Myr (SFR10 and SFR100), and those derived from UV plus IR luminosity (SFR$_{\rm UV+IR}$); Paβ-based SFRs, inferred by assuming no dust attenuation (SFR$^0_{\rm Pa\beta}$) and corrected for nebular attenuation (SFR$_{\rm Pa\beta}$), using the $A_{V,\rm neb}$ values reported in the last row (see Sect. 5.2 for details). $^{(\star)}$ $M_\star$ and SFRs of the bulge were computed by summing over the pixels within the bulge aperture and multiplying the resulting sum by two (see Sect. 4.2).

by up to a factor of 5 in integrated SED fitting, with larger offsets for higher specific SFRs. In the case of K20-ID7, outshining seems to play a minor role, given the smaller discrepancy between the resolved and integrated result. This discrepancy is more consistent with that found for star-forming galaxies of similar mass at $z \simeq 2$ (Shen et al. 2024) and at $z \simeq 4$–6 (Li et al. 2024; Lines et al. 2025).

To better constrain SFRs, stellar age, and dust attenuation, we performed an additional integrated SED fitting. This included the available photometry at longer wavelengths from *Spitzer*

IRAC (5.8 µm and 8 µm) and MIPS 24 µm, using the values reported by Dickinson et al. 2003 and Whitaker et al. 2014, as well as mid-IR data from *Herschel*/PACS 160 µm, for which we adopted the integrated photometry from Lutz et al. 2011. we also included ALMA Band 6 data at 1.2 mm, introduced in Sect. 2.4. In `CIGALE`, we modeled dust emission using dust templates from Dale et al. (2014) (see Appendix B for more details on the best-fit model).

As shown in Table 3 (see the column labeled Galaxy$_{1.2\mathrm{mm}}$), including mid- and far-IR photometry yields excellent agreement between the integrated $M_\star$ and its sum over pixels, as well as consistent $A_{V,\mathrm{star}}$ values. By contrast, the inferred SFR10 and SFR100 values are systematically lower than those from both resolved SED fitting and integrated modeling with photometry up to 4.4 µm. In particular, the resulting SFR10 is lower than the other two inferred total SFR10 values and the most accurate values previously published in Förster Schreiber et al. (2009) (SFR = 101–190 $\mathrm{M_\odot\,yr^{-1}}$; see Sect. 5 for details on previously published SFRs). Yet, the wide coverage of this photometric dataset, extending up to far-IR, allowed us to estimate the total SFR from the UV and IR luminosities of the SED best-fit model (Kennicutt 1998). Doing so, we obtained a higher SFR ($\mathrm{SFR_{UV+IR}} = 105 \pm 17\,\mathrm{M_\odot\,yr^{-1}}$), consistent with the sum over pixels. Investigating the causes of the systematic lower SFR10 derived from the integrated SED analysis with photometry up to 1.2 mm is beyond the scope of this paper.

5. 2D spatial distribution of Paβ line emission

5.1. Correction of Paβ line map for velocity gradients

Compared to long-slit spectroscopy, slitless grism observations allow us to recover the overall 2D emission line distribution after removing continuum emission (e.g., Nelson et al. 2016, 2024; Matharu et al. 2022). For high-resolution grism data of extended sources, such as NIRCam WFSS ($R \sim 1600$, FWHM $\approx 190\,\mathrm{km\,s^{-1}}$), the emission-line morphology along the dispersion axis combines spatial and velocity displacements. In contrast, low-resolution spectral data (e.g., HST/WFC3 or JWST/NIRISS, $R \sim 100$, FWHM $\approx 2000\,\mathrm{km\,s^{-1}}$) contain only spatial information along this dispersion axis. Consequently, accounting for this velocity-position degeneracy is a crucial, necessary step to recover the intrinsic 2D emission-line distribution or 1D line velocity profile from NIRCam WFSS data.

The left panel of Fig. 5 shows the continuum-subtracted Paβ emission line map of K20-ID7, reconstructed by the FRESCO team using `grizli` (Brammer 2023; see Oesch et al. 2023; Neufeld et al. 2024 for more details). This map was matched to the spatial resolution of the VLT/ERIS AO-assisted data (FWHM = 0.16″[11], compared to FWHM = 0.13″ for NIRCam F444W), using the `python` package `photutils.psf.matching`. The comparison with the continuum emission in the direct F444W image (white contours) clearly reveals a relative spatial offset with respect to Paβ line emission along the horizontal WE direction. Such offsets are fairly systematic and consistent with expectations, given the observed kinematics and orientation of the grism dispersion axis (with increasing wavelengths toward E). K20-ID7 indeed features a kinematic position angle of 25 deg (i.e., roughly aligned with the NE–SW direction) and a substantial velocity gradient (ranging from -300 to +300 km/s; Förster Schreiber et al. 2018; Genzel et al. 2023, Pulsoni et al., in prep.), as seen in the Hα kinematics from high-resolution IFU data. It follows that the largest offsets are observed at greater distances from the galaxy center along the kinematic major axis, where the velocity gradient is strongest. This can be well appreciated for the northernmost clump (i.e., Clump B, circled in red in the left and middle panels of Fig. 5). The fact that these offsets between the continuum and line emission are not observed in VLT/ERIS Hα data furthermore supports their nonphysical origin.

To break the spatial and kinematic degeneracy and recover the intrinsic Paβ spatial distribution, we relied on the (smoothed) Hα velocity map obtained from ERIS AO observations (Pulsoni et al., in prep.). Since Paβ and Hα emission originate from the same gas phase, we can reasonably assume the same kinematics for Paβ as for Hα. The mapping in NIRCam grism data is only weakly depends on wavelength and position, with a scale of 10.0 Å per NIRCam F444W pixel (i.e., 10.0 Å/0.063″). Given the 50 mas pixel scale of the 2D reconstructed Paβ map, a one-pixel shift results in a 7.9 Å wavelength-shift, which corresponds to $57\,\mathrm{km\,s^{-1}}$ at $\lambda \sim 4.13\,\mu$m (i.e., the observed Paβ wavelength for K20-ID7). To a first approximation, the velocity-corrected, intrinsic position along the spectral axis (i.e., x_{int}) of a given Paβ emitting pixel at a position x_{obs} in the reconstructed image can be recovered as

$$x_{\mathrm{int}} = x_{\mathrm{obs}} - v(x_{\mathrm{int}})/(57\,\mathrm{km\,s^{-1}}), \quad (1)$$

where $v(x_{\mathrm{int}})$ is the velocity for each pixel from the rotating disk model based on the ERIS Hα data (Pulsoni et al., in prep.).

The middle panel of Fig. 5 displays the reconstructed Paβ emission line map, after shifting each pixel along the horizontal (dispersion) axis according to Eq. (1). Although approximate, our velocity correction provides a much better spatial correspondence between the Paβ and continuum emission: the Paβ emission of the northernmost clump and the galaxy spiral arms now align well with the continuum emission seen in the F444W direct image. The Paβ line distribution reveals that most of the emission arises from the clumps and spiral arms. The S/N = 7 detection of the integrated Paβ line allows us to recover its spatial distribution with a significance of ∼5σ in the clumps and ∼3σ along the spiral arms, while the bulge and the other regions of the galaxy remain undetected in Paβ emission.

5.2. Star formation traced via Paβ line emission

We used the velocity-corrected Paβ map to spatially map recent star formation (with a timescale of ∼10 Myr), probing a more obscured regime compared to optical Balmer emission lines (e.g., Hα or Hβ). Following Reddy et al. (2023b), the SFR can be inferred from the dust-corrected Paβ luminosity ($L_{\mathrm{Pa}\beta}$) using their Eq. (2) (assuming $Z = 0.02$, the closest metallicity to our measurements):

$$\mathrm{SFR_{Pa\beta}[M_\odot/yr]} = 7.67 \times 10^{-41}\, L_{\mathrm{Pa}\beta}[\mathrm{erg/s}]. \quad (2)$$

Since we lack a full 2D map of nebular line attenuation and using $A_{V,\mathrm{star}}$ may introduce per-pixel correction errors (due to astrometric misalignments), in a first approximation we assumed negligible attenuation at the 1.28 µm Paβ wavelength and derived a SFR map from the observed (i.e., without dust correction) Paβ luminosity, through a pixel-by-pixel application of the equation above. The resulting Paβ-based SFR map is shown in the rightmost panel of Fig. 5. It has been rebinned to a 0.025″ pixel scale (to enable direct comparison with the SFR maps in Fig. 4)

[11] The Hα line map used in this work was smoothed to a spatial resolution of FWHM = 0.16″ (Pulsoni et al., in prep.), whereas the nominal resolution of the ERIS AO-assisted data is FWHM = 0.105″ (Förster Schreiber et al., in prep.).

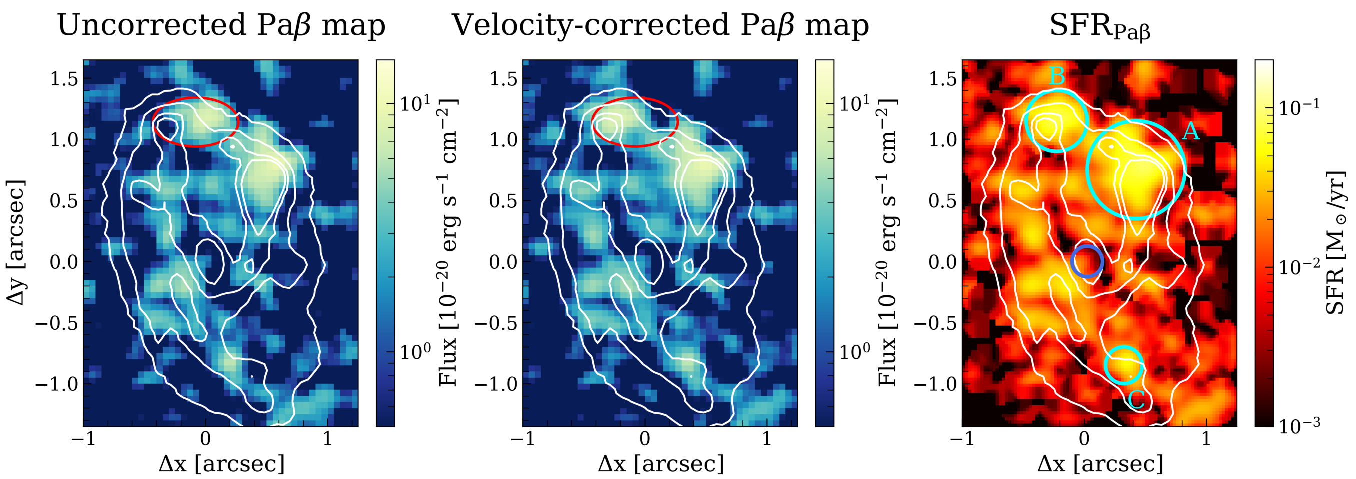

Fig. 5. 2D spatial distribution of Paβ in K20-ID7 from NIRCam grism F444W observations. *Left*: Paβ line map, as reconstructed by `grizli` (Brammer 2023), with white contours tracing the F444W continuum emission. The Paβ emission appears offset, with respect to the continuum emission, along the *x*-axis (i.e., the grism dispersion direction), due to velocity gradients. This is particularly evident for the northernmost clump (circled in red). *Middle*: Paβ line map after correcting for the Hα velocity-field model inferred from VLT/ERIS AO data (Pulsoni et al., in prep.). Here, the Paβ and continuum emission align more closely, as highlighted by their good spatial correspondence with the bright star-forming clumps detected at S/N = 5. *Right*: Paβ-traced SFR map, obtained by assuming negligible dust attenuation. Cyan circular apertures (diameters of 0.8″, 0.5″, and 0.3″) and a central blue aperture (0.25″) are used to infer the Paβ-based SFRs for the three brightest clumps and the bulge, respectively. The two Paβ maps have a 0.05″ pixel scale, while the SFR map is rebinned to a 0.025″ pixel scale and smoothed with a Gaussian kernel of σ = 1 pix.

and smoothed with a Gaussian kernel of σ =1 pixel. Table 3 reports the resulting total Paβ-based, not dust-corrected, SFRs (i.e., $\mathrm{SFR}^0_{\mathrm{Pa}\beta}$) obtained by summing the Paβ flux within dedicated circular apertures for Clumps A, B, and C (in cyan; diameters of 0.8″, 0.5″, 0.3″, respectively), as well as for the bulge (in red; diameter of 0.25″). A comparison of the SFR10 values derived from our resolved SED fitting (see Fig. 4 with those reported in Table 3) indicates that Paβ traces recent star formation in the clumps and spiral arm well, where extinction is low and the star formation is indeed recent. A major difference, however, arises for the central bulge, where the Paβ line emission is very weak. Consistent with the picture outlined in Sect. 4.2, this results from recent, low-level star formation and heavy extinction in the inner bulge regions, which remain significant even at the Paβ wavelength.

To place a robust lower limit on the Paβ flux in the bulge, we computed its expected value within our adopted bulge aperture, based on the SFR10 value from our SED modeling. We adopted two distinct values for dust attenuation: 1) stellar attenuation only, with $A_{V,\mathrm{star}} = 2.83 \pm 0.24$, and 2) extra nebular attenuation computed as $A_{V,\mathrm{neb}} = A_{V,\mathrm{star}}/0.44 = 6.43 \pm 0.55$ (Calzetti et al. 2000). We thus obtain lower limits for the expected observed Paβ flux, which translate into lower limits of $1.78\,\mathrm{M}_\odot\,\mathrm{yr}^{-1}$ and $0.076\,\mathrm{M}_\odot\,\mathrm{yr}^{-1}$ for the intrinsic Paβ-based SFR, both consistent with our $\mathrm{SFR}^0_{\mathrm{Pa}\beta}$ estimate obtained for the bulge aperture.

Finally, by fitting two Gaussian components to the 1D NIRCam WFSS spectrum (shown in Fig. 3), we infer a total Paβ flux of $F_{\mathrm{Pa}\beta} = (2.2 \pm 0.7) \times 10^{-17}\,\mathrm{erg\,s^{-1}\,cm^{-2}}$ for the whole galaxy, which yields a global $\mathrm{SFR}^0_{\mathrm{Pa}\beta} = (66 \pm 22)\,\mathrm{M}_\odot\,\mathrm{yr}^{-1}$. This total 1D Pa$\beta$ flux is more reliable than the sum of the Paβ fluxes over all pixels of the (velocity-corrected) Paβ line map, which adds noise from more diffuse galaxy regions. Compared to previous published estimates (Förster Schreiber et al. 2009), our inferred total $\mathrm{SFR}^0_{\mathrm{Pa}\beta}$ is systematically lower than the values derived from IR luminosity and integrated HST-based SED modeling ($\mathrm{SFR_{IR}} \simeq 101\,\mathrm{M}_\odot\,\mathrm{yr}^{-1}$ and $\mathrm{SFR_{SED}} \simeq 110\,\mathrm{M}_\odot\,\mathrm{yr}^{-1}$, respectively). Moreover, it is closer to the total Hα-traced SFR, which is corrected for stellar attenuation ($\mathrm{SFR}_{\mathrm{H}\alpha} \simeq 73\,\mathrm{M}_\odot\,\mathrm{yr}^{-1}$). This latter estimate is known to underestimate the true nebular attenuation (e.g., Calzetti et al. 2000; Price et al. 2014; Tacchella et al. 2018). By accounting for extra attenuation of nebular line emission, Förster Schreiber et al. (2009) found $\mathrm{SFR}_{\mathrm{H}\alpha} \simeq 190\,\mathrm{M}_\odot\,\mathrm{yr}^{-1}$. This result furthermore indicates that Paβ still suffers from substantial attenuation in more deeply obscured regions, such as the bulge. Therefore, neglecting extinction or improperly accounting for extra nebular attenuation at the 1.28 µm Paβ wavelength underestimates the intrinsic SFR of more obscured regions and, consequently, of the entire galaxy.

In Table 3, we report the local and total Paβ-based SFRs ($\mathrm{SFR}_{\mathrm{Pa}\beta}$) obtained by correcting for nebular attenuation derived from the hydrogen line ratios. Specifically, for Clumps A and B, and separately Clump C, we report the values respectively inferred for Clump-N and Clump-S from MSA spectra (see Table 2); for the bulge, we report the $A_{V,\mathrm{neb}}$ value inferred from $A_{V,\mathrm{star}}$; and for the whole galaxy, we report an average estimate based on medium- and broadband imaging (see Appendix C). As expected, the $\mathrm{SFR}_{\mathrm{Pa}\beta}$ of the clumps have not changed much with respect to the $\mathrm{SFR}^0_{\mathrm{Pa}\beta}$ values, due to their low extinction, whereas for the bulge and the whole galaxy, we obtain values consistent with those for SFR10. In particular, we note that the total $\mathrm{SFR}_{\mathrm{Pa}\beta}$ of the galaxy now also matches the global $\mathrm{SFR_{UV+IR}}$ estimate better.

6. Implications on the evolution of the galaxy disk

6.1. Hints for inside-out galaxy growth

As indicated in Sect. 4.2, the 2D stellar age map inferred from our resolved SED fitting reveals a relatively older stellar population in the bulge and the nearby regions and younger stellar populations in the clumps. Despite the large non-axisymmetry,

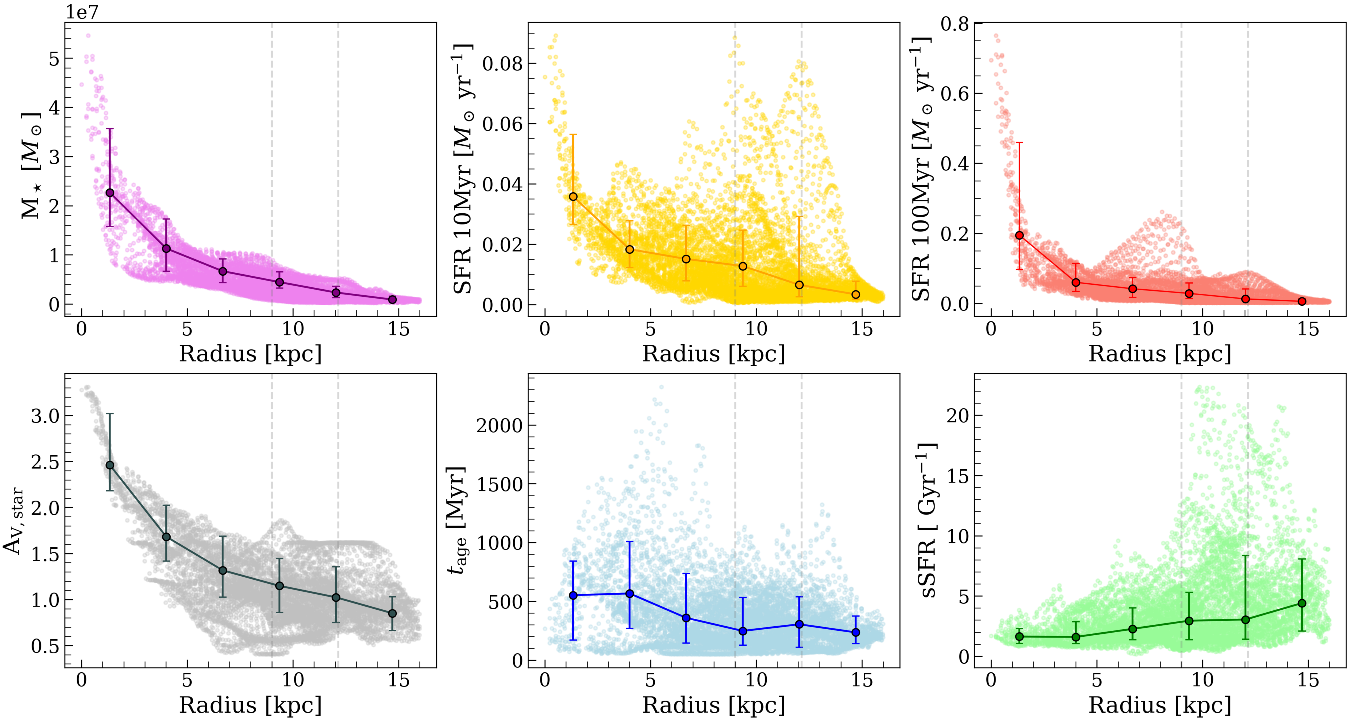

Fig. 6. Radial profiles of galaxy properties, as derived from our 2D SED-based maps. *Left to right, top*: Radial profiles of $M_\star$, SFR10, and SFR100. *Bottom*: $A_{V,\mathrm{star}}$, t_{age}, and specific SFR (sSFR = SFR10/$M_\star$). The big markers show the median value computed for each ring, with the error bars showing the $\pm1\sigma$ scatter. In the background, we plot the distribution of individual pixel values. The vertical dashed gray lines correspond to the de-projected radii of Clump A (~9 kpc) as well as Clumps B and C (~12 kpc).

we derived radial profiles for each physical parameter (Fig. 6) to better investigate radial trends of the various SED-inferred properties. These profiles are based on the resolved SED maps shown in Fig. 4, using six elliptical annuli at the galaxy's center and computed from the F444W image. Each annulus has a width of 0.25″ and is characterized by a semiminor to semimajor axis ratio of $b/a = 0.72$ (Genzel et al. 2023) and a position angle of 25° (counterclockwise from N to E; Förster Schreiber et al. 2018). As shown in Fig. 6, we computed the median value of the examined property in each elliptical annulus and associated it with an error equal to a $\pm1\sigma$ scatter. To also better appreciate azimuthal scatter, for each property we show the values of individual pixels as a function of their de-projected distance from the galaxy center, by correcting for the galaxy inclination (122°, Genzel et al. 2023).

The radial profiles overall highlight the presence of a massive, highly obscured yet star-forming bulge as also seen in other cosmic noon galaxies (Arriagada-Neira et al. 2025). Except for the specific SFR (sSFR = SFR10 / $M_\star$) and stellar age, all properties exhibit a declining median radial trend, with the clumps (vertical dashed lines) breaking down the azimuthal symmetry of the 2D SED maps and creating peaks in the scatter distribution. On the contrary, the sSFR features a slightly increasing median profile, reaching peaks in the scatter at the location of the clumps. The stellar age radial profile appears globally flat within the 1σ scatter, with typical uncertainties on pixel values of 50-70%. Yet, the stellar age radial profile tentatively exhibits a negative gradient, suggesting an older stellar population in the inner galaxy regions. We also notice that the stellar age map shown in Fig. 4 displays asymmetry between the northern and southern parts of the galaxy, which could furthermore contribute to washing out any possible age gradient. If this negative gradient is real, this would imply an inside-out growth for K20-ID7.

Even though our SED-based results cannot prove the inside-out growth of this galaxy, the available NIRSpec MSA spectroscopy independently supports this possible scenario. The detection of both Hα and the adjacent continuum emission in the PRISM/CLEAR data indeed allows us to locally estimate the rest-frame Hα equivalent width (EW), which is indicative of stellar population age (e.g., Levesque & Leitherer 2013). In particular, higher EWs indicate younger populations (Förster Schreiber et al. 2009, 2011; Reddy et al. 2018), since EW(Hα) depends on the ratio between the Hα line luminosity (a proxy of the current SFR) and the continuum luminosity (a proxy of the past star formation activity). Therefore, we can use the EW(Hα) as an independent age diagnostic to compare the stellar age trend resulting from our SED-based t_{age} map and radial gradient. In Fig. 7, we display the EW(Hα) as a function of the sSFR for each MSA shutter (same color code as in Fig. 2). In Fig. 7 we note a correlation between EW(Hα) and sSFR, such that regions with larger sSFRs also have higher EWs, as previously observed in individual galaxies at $z \approx 1-3$ (Reddy et al. 2018).

In terms of stellar age, the Clump-N and Ext-N regions exhibit higher EW(Hα) values (EW(Hα) ≈ 200 Å), hinting at the presence of a younger stellar population, compared to the inter-arm and Ext-SW shutters (EW(Hα) ≈ 90–100 Å). The Clump-S and Arm regions display intermediate values (despite the large EW(Hα) uncertainty for the latter) of EW(Hα) ≈ 140–170 Å. This relative trend is consistent with the tentative trend showed in our t_{age} map from resolved SED fitting (see Fig. 4). The older stellar population of the inter-arm region is also confirmed by the strong Balmer break in the corresponding PRISM/CLEAR spectrum (see Fig. 2). Although the distinct shutters probe galaxy regions of different natures (e.g., clumps, spiral arms, and inter-arm regions), considering their distance from the galaxy

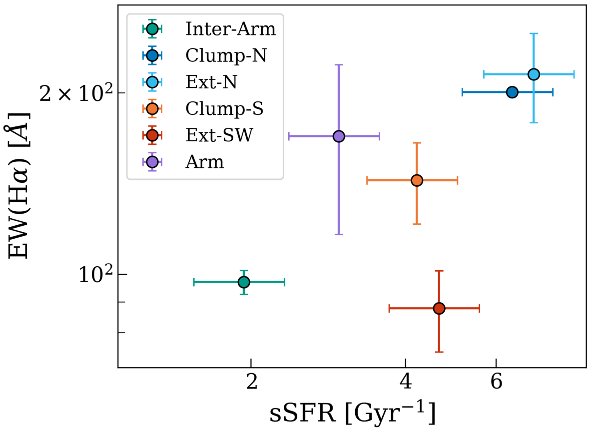

Fig. 7. Rest-frame EW(Hα) as a function of sSFR for the various galaxy regions probed by distinct MSA shutters. The EW(Hα) measurements are derived from PRISM/CLEAR data, while the sSFRs are derived from our SED-based SFR10 and $M_\star$ maps. The plot highlights a correlation between the two quantities, with higher EW(Hα) values scaling with higher sSFRs, indicative of younger stellar populations.

center, we find higher EW(Hα) values with increasing radii. Specifically, EW(Hα)$_{\rm Inter-Arm}$ < EW(Hα)$_{\rm Arm}$ < EW(Hα)$_{\rm Clump-N}$. This supports an "inside-out" formation scenario for K20-ID7 (Tacchella et al. 2015a; Nelson et al. 2016).

6.2. Connection with gas inflows

Exploiting high-resolution Hα SINFONI AO-assisted observations of K20-ID7, Genzel et al. (2023) find kinematic residuals indicative of rapid gas inflows at speeds of 87 km/s. More recent ERIS AO observations at higher spectral and spatial resolutions have confirmed the fast radial inflows and enabled a more accurate association with the spiral arms seen in NIRCam imaging (Pulsoni et al., in prep.). The detection of such radial gas inflows, along with the results inferred in this work, supports the scenario of inflowing gas funneled from the galaxy outskirts toward the central bulge, which dilutes the metal content of the galaxy. Radial gas inflows detected along spiral arms may be fueled by gas transport from the very outskirts of the disk and by external accretion from the circumgalactic medium (CGM). If the inflowing gas is pristine or metal-poor, this process is expected to leave imprints on the galaxy properties, as discussed in the following subsections.

6.2.1. "Diluted" gas phase metallicity

As mentioned in Sect. 3.2, the FMR predicts a metallicity of $12 + \log(\mathrm{O/H}) \approx 8.57$ (Curti et al. 2020b) for a galaxy with the same stellar mass and SFR as K20-ID7 (i.e., $M_\star \approx 4 \times 10^{10}\,\mathrm{M}_\odot$, $\mathrm{SFR}_{\mathrm{Pa}\beta} \simeq 120\,\mathrm{M}_\odot\,\mathrm{yr}^{-1}$). At such a high SFR, the relation between metallicity and $M_\star$ steepens. This has been interpreted to result from prominent dilution effects caused by large inflows of metal-poor gas (Curti et al. 2020b).

Additional evidence supporting dilution effects due to gas inflows comes from nitrogen abundance. The N/O derived in Sect. 3.3 (Table 2) is interestingly 0.3 dex higher at fixed metallicity than the best-fit relation measured for the local galaxies reported in Hayden-Pawson et al. (2022) and consistent with the large scatter observed a $z \sim 2$ (Shapley et al. 2015; Hayden-Pawson et al. 2022). In contrast to oxygen and sulfur – α elements mainly produced on shorter timescales as core collapse supernovae (CCSNe) explode – nitrogen has two different creation channels (see Kobayashi & Taylor 2023, for a review): a primary, metallicity-independent channel, in which nitrogen is expelled by CCSNe (Maiolino & Mannucci 2019), and a secondary channel, in which nitrogen originates from intermediate-mass, metal-rich stars in the asymptotic giant branch phase, which dominate nitrogen production at high metallicity (e.g., Vincenzo et al. 2016). Given the different formation mechanisms of nitrogen compared to oxygen, measuring its abundance provides insights into the star formation and chemical enrichment histories of the galaxy (Sanders et al. 2023).

With the advent of JWST, nitrogen enhancement is found to be common in very metal-poor ($Z \sim 0.1\,Z_\odot$) and high-z ($z > 4$) star-forming galaxies (e.g., Bunker et al. 2023; Cameron et al. 2023; Isobe et al. 2023; Topping et al. 2024), though it is not ubiquitous (Rogers et al. 2024). Various mechanisms were proposed to explain such nitrogen enhancement, including an excess of Wolf-Rayet stars (Flury et al. 2025; Welch et al. 2025), varying IMFs (Arellano-Córdova et al. 2025), and enrichment by population III stars (Nandal et al. 2024). Considering the inflow detection in K20-ID7 (Genzel et al. 2023, Pulsoni et al., in prep.), we may be witnessing an overall gas–metallicity dilution, as traced by O/H, rather than a nitrogen enhancement (e.g., Stiavelli et al. 2025). The overabundance of N/O relative to subsolar O/H may arise from lower-metallicity gas from the disk outskirts or external accretion, which dilutes the gas-phase oxygen abundance in the disk while preserving the relative N/O abundance.

6.2.2. Low-metallicity clumps

Cosmological simulations show that gas inflows from the CGM are often associated with off-center star-forming clumps, bright in Hα and poor in metals (Ceverino et al. 2016). As reported in Sect. 3.2, we find no significant difference in the metallicity of the clumps compared to that in the other probed galaxy regions. Yet, we note that prominent metallicity gradients are smoothed due to the spatial extent of the MSA shutters. In particular, we expect a large amount of metals to be ejected during the explosion of massive stars in Clump-N due to intense star formation ($\sim 20\,\mathrm{M}_\odot\,\mathrm{yr}^{-1}$), contrary to observations. Indeed, Clump-N is found in the same region as the strongest inflow detection (Genzel et al. 2023; Pulsoni et al., in prep.). This suggests the clump may have an intrinsic metallicity lower than that inferred from the Clump-N MSA data, which reduces the O/H abundance due to pristine gas accretion, while replenishing the star-forming region with gas.

Estimating the amount of pristine gas needed to produce a given observed decrease in metallicity involves assuming an infall model, where the pristine inflowing gas is responsible for diluting metallicity and boosting star formation. By using Eq. (8) from Mannucci et al. (2010) and assuming a decreased metallicity of only 0.1 dex for Clump-N, we find that the accreted pristine gas in the clump should account for 20% of the mass of the gas. This would explain such a decrease in metallicity. Assuming a gas fraction of $M_{\rm gas}/M_\star = 1.8$ (Genzel et al. 2023), and considering our inferred stellar mass ($M_\star \approx 4 \times 10^{10}\,\mathrm{M}_\odot$), we estimate that the pristine gas accreted on the clump is on the order of $10^9\,M_\odot$. Clump-S is also located in a region where kinematic residuals indicate the presence of gas inflows. Applying similar reasoning for Clump-N, accretion of $\sim 10^8\,M_\odot$ of pristine gas would be required to account for a 0.1 dex dilution.

6.3. Sulfur abundance at $z = 2.2$

The detection of the [SII] and [SIII] emission lines in the NIRSpec MSA spectra allowed us to locally measure the sulfur abundance of K20-ID7 (in Sect. 3.3), which had previously been determined only for a handful of galaxies at $z > 1$ (e.g., Sanders et al. 2020; Rogers et al. 2024, 2026). Before the advent of JWST, detecting the [SIII] emission lines at $z \gtrsim 1.5$ was indeed challenging, because they are emitted at the boundary between optical and near-IR wavelengths; hence, they are redshifted outside the atmospheric transmission windows accessible from the ground. Sulfur is an α element (similar to oxygen), mainly produced inside the core of massive stars and returned to the ISM on short timescales through the explosion of CCSNe. Contrary to nitrogen, S/O typically does not depend on galactic metallicity or SFH, but rather on supernova yields only. Hence, it is usually assumed to be constant throughout cosmic time and close to the solar value ($\log(\text{S/O})_{\odot} \sim -1.7$; Asplund et al. 2009).

In Sect. 3.3, we reported a value of log(S/O) -2.0 ± 0.2 and -1.9 ± 0.2 for the inter-arm and Clump-N regions of K20-ID7. The measured value is systematically lower than the solar value of $\log(\text{S/O})_{\odot} \sim -1.6$ (Asplund et al. 2021). For Clump-S, we still obtain a subsolar S/O abundance compatible with the solar value within the large uncertainties. A low S/O abundance is also observed in other $z > 2$ galaxies (Rogers et al. 2024, 2026) at both low- and high-metallicities. The inferred abundance pattern may result from a secondary (subdominant) sulfur production channel through type Ia SNe (Kobayashi et al. 2020), which produces different oxygen and sulfur yields, thereby altering the relative S/O abundance. The subsolar nature of these high-z sources, hence, might indicate that type Ia SNe have not had time to explode yet. Another possible explanation for the low S/O values is that sulfur may be captured by ice and dust grains (Hily-Blant et al. 2022; Pérez-Díaz et al. 2024). Studies of local galaxies and individual HII regions have found large scatters for S/O abundance (e.g., Díaz & Zamora 2022; Pérez-Díaz et al. 2024), with some studies revealing tentative evidence of lower S/O at increasing 12 + log(O/H) (Díaz & Zamora 2022), while others find no such trend (Izotov et al. 2006). However, a similar decreasing trend with metallicity is also observed for other α elements, which may be ascribed to the depletion of oxygen into dust grains (Izotov et al. 2006). In light of this, our measurements of abundance patterns in K20-ID7 highlight the need for caution when using nitrogen or sulfur to infer 12 + log(O/H) gas-phase metallicities (Pérez-Díaz et al. 2024). In particular, larger samples of $z > 1$ galaxies with available S/O measurements are needed to validate the assumption of constant S/O abundance at high redshifts.

7. Conclusions

Relying on a novel set of JWST observations of K20-ID7, including both NIRSpec and NIRCam data, this work presents a comprehensive resolved study of the ISM and stellar population properties of K20-ID7, a large star-forming galaxy at $z = 2.224$ with an outstanding spiral morphology. In doing so, our analysis leverages the synergy between JWST and ground-based IFU AO observations and introduces two key novelties in the data reduction of NIRSpec MSA spectra and in the post-processing of NIRCam WFSS data: 1) the extraction of science spectra from multiple MSA shutters – not just the central one (as in the standard reduction procedure) – thereby probing seven distinct galaxy regions in total; the recovery of the intrinsic 2D spatial distribution of the Paβ line emission, achieved by correcting the Paβ line map reconstructed from NIRCam WFSS data for velocity gradients. This correction uses the Hα velocity-field model derived from IFU ERIS AO data at a high spectral resolution ($R \sim 10\,500$) and comparable spatial resolution (Pulsoni et al., in prep.). Below, we summarize the main results of this work:

- By means of different emission-line diagnostics, we investigated the ISM properties in three distinct galaxy regions, i.e., two clumps and an inter-arm region. Overall, we found the clumps to exhibit lower dust attenuation ($A_{V,\text{neb}} \simeq 0.4$), and feature relatively low electron densities ($n_e \lesssim 300$ cm^{-3}) and ionization parameters ($\log(U) \simeq -3.0$). As inferred from our resolved SED analysis, the clumps are found to be massive ($M_\star = 0.67$–3.5×10^9 M$_\odot$) and have SFRs ranging from 3–20 M$_\odot$ yr^{-1}. The inter-arm region is more dust-attenuated ($A_{V,\text{neb}} \simeq 1.3$) and has similar ionization conditions to those of the clumps. For this region, we derived a 2σ upper limit on the electron density of $n_e < 1900$ cm^{-3}.
- In the same regions, we also explored the gas-phase metallicity 12 + log(O/H), by using strong-line diagnostics as well as nitrogen and sulfur chemical abundances. We also obtained a metallicity measurement for a fourth region, corresponding to a spiral arm. We find no statistically significant difference in metallicity between the various regions, featuring 12 + log(O/H) values in the 8.49–8.58 range and uncertainties of about 0.1–0.2 dex overall.
- We find evidence of metallicity patterns that are likely imprints of the known gas inflows detected in K20-ID7 (Genzel et al. 2023; Pulsoni et al., in prep.). Our inferred metallicity values are compatible with the FMR-expected metallicity (i.e., 12 + log(O/H) ≈ 8.57) for a galaxy with the same stellar mass and SFR as those derived for K20-ID7 (i.e., $M_\star \approx 4 \times 10^{10}$ M$_\odot$, SFR$_{\text{Pa}\beta} \simeq 120$ M$_\odot$ yr^{-1}). At such high SFRs, the steepening of the $Z - M_\star$ relation indicates dilution effects due to gas inflows of metal-poor gas. Similarly, such diluted metallicity could also explain the observed 0.3 dex enhancement in the log(N/O) abundance (i.e., $\simeq$-1) in the log(N/O) – 12 + log(O/H) plane.
- Given the [SII] and [SIII] emission lines detected in the NIRSpec MSA data, we measured the sulfur abundance in the inter-arm and clump regions (12 + log(S/H) of $6.6^{+0.2}_{-0.2}$ for the first two, and $6.7^{+0.3}_{-0.2}$ for the third one). When combined with the 12 + log(O/H) values, these yield a relative log(S/O) = -1.9, which is lower than the expected constant (solar) value (i.e., log(S/O) ≈ -1.7), yet consistent within the uncertainties. This might indicate a secondary production channel for sulfur via the explosion of type I SNe on longer timescales.
- The 2D map of stellar age, derived from our resolved SED fitting, and the extracted radial profile tentatively show a negative gradient, with older stellar populations on average closer to the center ($t_{\text{age}} \approx 400 - 2000$ Myr) and younger ones in the outer regions (particularly in the clumps, $t_{\text{age}} = 50$–100 Myr). This trend is also supported by an inverse increasing trend in sSFR, and the Hα EWs inferred from the NIRSpec MSA spectra for distinct galaxy regions.
- Our resolved SED analysis, along with the velocity-corrected Paβ line map, reveals a central moderately massive ($M_\star = (7 \pm 3) \times 10^9$ M$_\odot$) bulge, which is highly obscured ($A_{V,\text{neb}} = 6.43 \pm 0.55$) and undetected in line emission at the 1.28 µm Paβ wavelength. The bulge exhibits recent (~10 Myr) star formation (SFR10$_{\text{Bulge}} = 12 \pm 8$ M$_\odot$ yr^{-1}), and even a higher activity in the past (SFR100$_{\text{Bulge}} = 82 \pm 42$ M$_\odot$ yr^{-1}). Together with the relatively older stellar ages in the inner galaxy regions ($t_{\text{age}} \approx 400$–$2000$ Myr), the enhanced SFR100 of the bulge supports the scenario that it assembled most of

its stellar mass in the past, while maintaining some level of active star formation.

Taking advantage of the synergy between deep ground-based AO IFU observations, this work showcases the crucial role that JWST can play in investigating key galaxy formation and evolution processes at cosmic noon. Moreover, the successful analysis of K20-ID7 presented in this work paves the way for similar studies of larger samples of galaxies at cosmic noon, leveraging available spectroscopy from JWST and ground-based IFU facilities. This will enable an accurate, complete, and resolved characterization of the ISM and stellar population properties. Moreover, the discovery of the deeply obscured yet star-forming bulge in K20-ID7 underscores the importance of future high-resolution millimeter continuum observations with ALMA. Such observations would detect obscured star formation activity in the bulge and pin down its current growth rate.

Acknowledgements. The authors are grateful to S. Carniani for valuable comments and discussion. G.T., N.M.F.S., C.B., J.C. and J.M.E.S. acknowledge funding by the European Union (ERC Advanced Grant GALPHYS, 101055023), H.Ü. and G.M. acknowledge funding by the European Union (ERC APEX, 101164796). Views and opinions expressed are, however, those of the authors only and do not necessarily reflect those of the European Union or the European Research Council. Neither the European Union nor the granting authority can be held responsible for them. L.S. acknowledges financial support from the PhD grant funded on PNRR Funds Notice No. 3264 28-12-2021 PNRR M4C2 Reference IR0000034 STILES Investment 3.1 CUP C33C22000640006. This work has been financed by the European Union with the Next Generation EU plan, Mission 4, through PRIN-MUR project "PROMETEUS" (202223XPZM), CUP C53D2300080-006. This work is based on observations made with the NASA/ESA/CSA James Webb Space Telescope. Some of the data were obtained from the Mikulski Archive for Space Telescopes at the Space Telescope Science Institute, which is operated by the Association of Universities for Research in Astronomy, Inc., under NASA contract NAS 5-03127 for JWST. These observations are associated with programs: 1210, 1895, 1180, 6541. Some of the data products presented herein were retrieved from the Dawn JWST Archive (DJA). DJA is an initiative of the Cosmic Dawn Center (DAWN), which is funded by the Danish National Research Foundation under grant DNRF140. This work was supported by the Open Access Publishing Fund of the Scuola Normale Superiore.

References

Arellano-Córdova, K. Z., Cullen, F., Carnall, A. C., et al. 2025, MNRAS, 540, 2991
Arriagada-Neira, S., Herrera-Camus, R., Villanueva, V., et al. 2025, A&A, 696, A83
Ashby, M. L. N., Willner, S. P., Fazio, G. G., et al. 2013, ApJ, 769, 80
Asplund, M., Grevesse, N., Sauval, A. J., & Scott, P. 2009, ARA&A, 47, 481
Asplund, M., Amarsi, A. M., & Grevesse, N. 2021, A&A, 653, A141
Boquien, M., Burgarella, D., Roehlly, Y., et al. 2019, A&A, 622, A103
Brammer, G. 2019, Astrophysics Source Code Library [record ascl:1905.001]
Brammer, G. 2023, grizli
Brammer, G. B., van Dokkum, P. G., Franx, M., et al. 2012, ApJS, 200, 13
Bruzual, G., & Charlot, S. 2003, MNRAS, 344, 1000
Bunker, A. J., Saxena, A., Cameron, A. J., et al. 2023, A&A, 677, A88
Bunker, A. J., Cameron, A. J., Curtis-Lake, E., et al. 2024, A&A, 690, A288
Calzetti, D., Armus, L., Bohlin, R. C., et al. 2000, ApJ, 533, 682
Cameron, A. J., Katz, H., Rey, M. P., & Saxena, A. 2023, MNRAS, 523, 3516
Caon, N., Capaccioli, M., & D'Onofrio, M. 1993, MNRAS, 265, 1013
Cappellari, M. 2023, MNRAS, 526, 3273
Carniani, S., Hainline, K., D'Eugenio, F., et al. 2024, Nature, 633, 318
Ceverino, D., Sánchez Almeida, J., Muñoz Tuñón, C., et al. 2016, MNRAS, 457, 2605
Chabrier, G. 2003, PASP, 115, 763
Curti, M., Maiolino, R., Cirasuolo, M., et al. 2020a, MNRAS, 492, 821
Curti, M., Mannucci, F., Cresci, G., & Maiolino, R. 2020b, MNRAS, 491, 944
Curtis-Lake, E., Carniani, S., Cameron, A., et al. 2023, Nat. Astron., 7, 622
Dale, D. A., Helou, G., Magdis, G. E., et al. 2014, ApJ, 784, 83
Davies, R. L., Förster Schreiber, N. M., Genzel, R., et al. 2021, ApJ, 909, 78
Davies, R., Absil, O., Agapito, G., et al. 2023, A&A, 674, A207
D'Eugenio, F., Cameron, A. J., Scholtz, J., et al. 2025, ApJS, 277, 4
Díaz, Á. I., & Zamora, S. 2022, MNRAS, 511, 4377
Díaz, A. I., Castellanos, M., Terlevich, E., & Luisa García-Vargas, M. 2000, MNRAS, 318, 462
Díaz, Á. I., Terlevich, E., Castellanos, M., & Hägele, G. F. 2007, MNRAS, 382, 251
Dickinson, M., Giavalisco, M., & GOODS Team 2003, in The Mass of Galaxies at Low and High Redshift, eds. R. Bender, & A. Renzini, 324
Eisenhauer, F., Abuter, R., Bickert, K., et al. 2003, in Instrument Design and Performance for Optical/Infrared Ground-based Telescopes, eds. M. Iye, & A. F. M. Moorwood, SPIE Conf. Ser., 4841, 1548
Eisenstein, D. J., Willott, C., Alberts, S., et al. 2026, ApJS, 283, 6
Espejo Salcedo, J. M., Glazebrook, K., Fisher, D. B., et al. 2025a, MNRAS, 536, 1188
Espejo Salcedo, J. M., Pastras, S., Vácha, J., et al. 2025b, A&A, 700, A42
Ferreira, L., Conselice, C. J., Sazonova, E., et al. 2023, ApJ, 955, 94
Ferruit, P., Jakobsen, P., Giardino, G., et al. 2022, A&A, 661, A81
Finkelstein, S. L., Bagley, M. B., Ferguson, H. C., et al. 2023, ApJ, 946, L13
Flury, S. R., Arellano-Córdova, K. Z., Moran, E. C., & Einsig, A. 2025, MNRAS, 543, 3367
Förster Schreiber, N. M., & Wuyts, S. 2020, ARA&A, 58, 661
Förster Schreiber, N. M., Genzel, R., Bouché, N., et al. 2009, ApJ, 706, 1364
Förster Schreiber, N. M., Shapley, A. E., Genzel, R., et al. 2011, ApJ, 739, 45
Förster Schreiber, N. M., Renzini, A., Mancini, C., et al. 2018, ApJS, 238, 21
Förster Schreiber, N. M., Übler, H., Davies, R. L., et al. 2019, ApJ, 875, 21
Genzel, R., Newman, S., Jones, T., et al. 2011, ApJ, 733, 101
Genzel, R., Förster Schreiber, N. M., Rosario, D., et al. 2014, ApJ, 796, 7
Genzel, R., Jolly, J. B., Liu, D., et al. 2023, ApJ, 957, 48
Giavalisco, M., Ferguson, H. C., Koekemoer, A. M., et al. 2004, ApJ, 600, L93
Giménez-Arteaga, C., Oesch, P. A., Brammer, G. B., et al. 2023, ApJ, 948, 126
Giménez-Arteaga, C., Fujimoto, S., Valentino, F., et al. 2024, A&A, 686, A63
Grogin, N. A., Kocevski, D. D., Faber, S. M., et al. 2011, ApJS, 197, 35
Hayden-Pawson, C., Curti, M., Maiolino, R., et al. 2022, MNRAS, 512, 2867
Hily-Blant, P., Pineau des Forêts, G., Faure, A., & Lique, F. 2022, A&A, 658, A168
Isobe, Y., Ouchi, M., Tominaga, N., et al. 2023, ApJ, 959, 100
Izotov, Y. I., Stasińska, G., Meynet, G., Guseva, N. G., & Thuan, T. X. 2006, A&A, 448, 955
Jakobsen, P., Ferruit, P., Alves de Oliveira, C., et al. 2022, A&A, 661, A80
Ju, M., Wang, X., Jones, T., et al. 2025, ApJ, 978, L39
Kalita, B. S., Suzuki, T. L., Kashino, D., et al. 2025, MNRAS, 536, 3090
Kashino, D., Lilly, S. J., Matthee, J., et al. 2023, ApJ, 950, 66
Kennicutt, R. C., Jr 1998, ARA&A, 36, 189
Kennicutt, R. C., & Evans, N. J. 2012, ARA&A, 50, 531
Kobayashi, C., & Taylor, P. 2023, arXiv e-prints [arXiv:2302.07255]
Kobayashi, C., Karakas, A. I., & Lugaro, M. 2020, ApJ, 900, 179
Koekemoer, A. M., Faber, S. M., Ferguson, H. C., et al. 2011, ApJS, 197, 36
Kormendy, J., & Kennicutt, R. C., Jr 2004, ARA&A, 42, 603
Lang, P., Wuyts, S., Somerville, R. S., et al. 2014, ApJ, 788, 11
Levesque, E. M., & Leitherer, C. 2013, ApJ, 779, 170
Li, J., Da Cunha, E., González-López, J., et al. 2024, ApJ, 976, 70
Lines, N. E. P., Bowler, R. A. A., Adams, N. J., et al. 2025, MNRAS, 539, 2685
Lorenz, B., Suess, K. A., Kriek, M., et al. 2025, ApJ, 988, L20
Lutz, D., Poglitsch, A., Altieri, B., et al. 2011, A&A, 532, A90
Madau, P., & Dickinson, M. 2014, ARA&A, 52, 415
Maiolino, R., & Mannucci, F. 2019, A&ARv, 27, 3
Mannucci, F., Cresci, G., Maiolino, R., Marconi, A., & Gnerucci, A. 2010, MNRAS, 408, 2115
Maraston, C., Pforr, J., Renzini, A., et al. 2010, MNRAS, 407, 830
Markov, V., Gallerani, S., Ferrara, A., et al. 2025, Nat. Astron., 9, 458
Masters, D., Faisst, A., & Capak, P. 2016, ApJ, 828, 18
Matharu, J., Papovich, C., Simons, R. C., et al. 2022, ApJ, 937, 16
Naidu, R. P., Oesch, P. A., Brammer, G., et al. 2026, Open J. Astrophys., 9, 56033
Nandal, D., Regan, J. A., Woods, T. E., et al. 2024, A&A, 683, A156
Nelson, E. J., van Dokkum, P. G., Förster Schreiber, N. M., et al. 2016, ApJ, 828, 27
Nelson, E., Brammer, G., Giménez-Arteaga, C., et al. 2024, ApJ, 976, L27
Nestor Shachar, A., Sternberg, A., Genzel, R., et al. 2025, ApJ, 988, 182
Neufeld, C., van Dokkum, P., Asali, Y., et al. 2024, ApJ, 972, 156
Oesch, P. A., Brammer, G., Naidu, R. P., et al. 2023, MNRAS, 525, 2864
Osterbrock, D. E., & Ferland, G. J. 2006, Astrophysics of Gaseous Nebulae and Active Galactic Nuclei (Sausalito, CA: University Science Books)
Park, M., Belli, S., Conroy, C., et al. 2024, ApJ, 976, 72
Peng, C. Y., Ho, L. C., Impey, C. D., & Rix, H.-W. 2002, AJ, 124, 266
Pérez-Díaz, B., Pérez-Montero, E., Fernández-Ontiveros, J. A., et al. 2024, A&A, 685, A168
Pilyugin, L. S., Vílchez, J. M., Mattsson, L., & Thuan, T. X. 2012, MNRAS, 421, 1624
Planck Collaboration XIII. 2016, A&A, 594, A13
Price, S. H., Kriek, M., Brammer, G. B., et al. 2014, ApJ, 788, 86
Reddy, N. A., Shapley, A. E., Sanders, R. L., et al. 2018, ApJ, 869, 92

Reddy, N. A., Topping, M. W., Sanders, R. L., Shapley, A. E., & Brammer, G. 2023a, ApJ, 952, 167
Reddy, N. A., Topping, M. W., Sanders, R. L., Shapley, A. E., & Brammer, G. 2023b, ApJ, 948, 83
Reddy, N. A., Shapley, A. E., Sanders, R. L., et al. 2026, ApJ, 999, 15
Rieke, M. J., Kelly, D. M., Misselt, K., et al. 2023, PASP, 135, 028001
Rogers, N. S. J., Strom, A. L., Rudie, G. C., et al. 2024, ApJ, 964, L12
Rogers, N. S. J., Strom, A. L., Rudie, G. C., et al. 2026, ApJ, 997, L44
Sanders, R. L., Shapley, A. E., Kriek, M., et al. 2016, ApJ, 816, 23
Sanders, R. L., Jones, T., Shapley, A. E., et al. 2020, ApJ, 888, L11
Sanders, R. L., Shapley, A. E., Clarke, L., et al. 2023, ApJ, 943, 75
Sanders, R. L., Shapley, A. E., Topping, M. W., et al. 2025, arXiv e-prints [arXiv:2508.10099]
Scholtz, J., Carniani, S., Parlanti, E., et al. 2025, arXiv e-prints [arXiv:2510.01034]
Shapley, A. E., Reddy, N. A., Kriek, M., et al. 2015, ApJ, 801, 88
Shen, L., Papovich, C., Matharu, J., et al. 2024, ApJ, 963, L49
Skelton, R. E., Whitaker, K. E., Momcheva, I. G., et al. 2014, ApJS, 214, 24
Slob, M., Kriek, M., de Graaff, A., et al. 2025, A&A, 702, A110
Sorba, R., & Sawicki, M. 2018, MNRAS, 476, 1532
Speagle, J. S., Steinhardt, C. L., Capak, P. L., & Silverman, J. D. 2014, ApJS, 214, 15
Steidel, C. C., Strom, A. L., Pettini, M., et al. 2016, ApJ, 826, 159
Stiavelli, M., Morishita, T., Chiaberge, M., et al. 2025, ApJ, 981, 136
Strom, A. L., Steidel, C. C., Rudie, G. C., Trainor, R. F., & Pettini, M. 2018, ApJ, 868, 117
Sunnquist, B., Boyer, M., Brooks, B., et al. 2025, Version 4 of the NIRCam Wisp Templates: Wisp Characterization, Stability, and Validation Testing, Technical Report JWST-STScI-009225
Tacchella, S., Carollo, C. M., Renzini, A., et al. 2015a, Science, 348, 314
Tacchella, S., Lang, P., Carollo, C. M., et al. 2015b, ApJ, 802, 101
Tacchella, S., Carollo, C. M., Förster Schreiber, N. M., et al. 2018, ApJ, 859, 56
Tacconi, L. J., Genzel, R., & Sternberg, A. 2020, ARA&A, 58, 157
Toomre, A. 1964, ApJ, 139, 1217
Topping, M. W., Stark, D. P., Senchyna, P., et al. 2024, MNRAS, 529, 3301
Topping, M. W., Sanders, R. L., Shapley, A. E., et al. 2025, MNRAS, 541, 1707
Valentino, F., Brammer, G., Gould, K. M. L., et al. 2023, ApJ, 947, 20
Vazdekis, A., Sánchez-Blázquez, P., Falcón-Barroso, J., et al. 2010, MNRAS, 404, 1639
Vincenzo, F., Belfiore, F., Maiolino, R., Matteucci, F., & Ventura, P. 2016, MNRAS, 458, 3466
Walter, F., Carilli, C., Neeleman, M., et al. 2020, ApJ, 902, 111
Welch, B., Rivera-Thorsen, T. E., Rigby, J. R., et al. 2025, ApJ, 980, 33
Whitaker, K. E., Franx, M., Leja, J., et al. 2014, ApJ, 795, 104
Wuyts, S., Förster Schreiber, N. M., Genzel, R., et al. 2012, ApJ, 753, 114
Wuyts, S., Förster Schreiber, N. M., Nelson, E. J., et al. 2013, ApJ, 779, 135

[1] Max-Planck-Institut für extraterrestrische Physik (MPE), Gießenbachstraße 1, 85748 Garching, Germany
[2] Scuola Normale Superiore, Piazza dei Cavalieri 7, I-56126 Pisa, Italy
[3] Department of Physics and Astronomy "Augusto Righi", University of Bologna, Via Piero Gobetti 93/2, I-40129 Bologna, Italy
[4] INAF – Astrophysics and Space Science Observatory of Bologna, Via Piero Gobetti 93/3, I-40129 Bologna, Italy
[5] Max-Planck-Institut für Astrophysik (MPA), Karl-SchwarzschildStr. 1, D-85748 Garching, Germany
[6] Department of Astronomy, University of Geneva, Chemin Pegasi 51, CH1290 Versoix, Switzerland
[7] Cosmic Dawn Center (DAWN), Niels Bohr Institute, University of Copenhagen, Jagtvej 128, DK-2200 København N, Denmark
[8] European Southern Observatory, Karl-Schwarzschild-Str. 2, 85748 Garching bei München, Germany
[9] INAF – Osservatorio Astrofisico di Arcetri, Largo E. Fermi 5, I-50125 Florence, Italy
[10] Department of Physics, Technical University of Munich, 85748 Garching, Germany
[11] Departments of Physics and Astronomy, University of California, Berkeley, CA 94720, USA
[12] Departamento de Astronomía, Universidad de Concepción, Barrio Universitario, Concepción, Chile
[13] DTU-Space, Technical University of Denmark, Elektrovej 327, DK2800 Kgs. Lyngby, Denmark
[14] Purple Mountain Observatory, Chinese Academy of Sciences, 10 Yuanhua Road, Nanjing 210023, China
[15] School of Physics and Astronomy, Tel Aviv University, Tel Aviv 69978, Israel
[16] Space Telescope Science Institute (STScI), 3700 San Martin Drive, Baltimore, MD 21218, USA
[17] Osservatorio Astronomico di Padova, Vicolo dell'Osservatorio 5, Padova I-35122, Italy
[18] University of Trento, Via Sommarive 14, Trento I-38123, Italy
[19] Dipartimento di Fisica e Astronomia, Università di Firenze, Via G. Sansone 1, I-50019 Sesto F.no (Firenze), Italy
[20] Department of Physics, University of Bath, Claverton Down, Bath BA2 7AY, UK

Appendix A: Spectral fitting of NIRSpec MSA data

In this appendix, we provide details on the spectral fitting of the NIRSpec MSA spectra of K20-ID7, at low spectral resolution and separately for the medium- and high-resolution gratings. In the PRISM/CLEAR spectra, stellar continuum is well detected and close emission lines are blended together (e.g., Hβ+ [OIII], Hα + [NII], [SII] line doublet). On the contrary, in medium- and high-resolution data continuum emission is faint and the emission lines are separately detected, although spectrally resolved only with the high-resolution ($R \sim 2700$) grating G395H/F290LP. The best-fit results obtained for the emission lines detected at $S/N > 3$ are listed in Table A.1, separately for data at different spectral resolution. Lines simultaneously observed with different gratings have mostly fluxes consistent within the errors, or they differ by less than $\sim 20\%$, compatible with the known (undesired) differences in the flux calibration at different resolution (e.g., D'Eugenio et al. 2025). For this reason, we caution on the absolute value of the inferred line fluxes, which should preferably be used for a relative comparison between different galaxy regions.

A.1. Low-resolution spectra

As shown in Fig. 2, the PRISM/CLEAR spectra of K20-ID7 exhibit a prominent continuum emission (especially Clump-N, Clump-S, and Inter-Arm), in addition to numerous (spectrally unresolved) emission lines. We fit the full (continuum plus emission lines) spectra by means of the Penalized PiXel-Fitting code (pPXF; Cappellari 2023), which models continuum emission through a linear combination of simple stellar population (SSP) models, and emission lines by means of Gaussian components. We use stellar templates from the MILES SSP library (Vazdekis et al. 2010), and constrain all emission lines to have the same kinematics (i.e., velocity and velocity dispersion). The line ratios of [OIII]λ5007/[OIII]λ4959 and [NII]λ6584/[NII]λ6548 are also fixed to 2.98 and 2.94, respectively, according to atomic physics prescriptions (see Osterbrock & Ferland 2006). The best-fit continuum emission is then used as a continuum input for the subsequent fitting of the emission lines.

After this first fitting with pPXF, we subtract the best-fit continuum model from the data and perform a refined modeling of the emission lines only, with a custom python script to properly account for the poor and variable spectral resolution of the PRISM/CLEAR data (varying from R$\sim$30 at $\sim$1.1μm to R$\sim$400 at the reddest wavelength; see Jakobsen et al. 2022), and accurately estimate the flux of the emission lines and the relative error. As done in the previous fitting with pPXF, we constrain all lines to the same velocity and fit [OIII] and [NII] line doublets with a fixed line ratio. To account for the varying spectral resolution of the PRISM data, we tie the velocity dispersion only between lines that are close in wavelength (e.g., [OIII] and Hβ). Moreover, due to the poor spectral resolution of PRISM data (i.e., $R = 100$), [NII] and Hα emission lines appear blended together. Since they are separately resolved in the medium-resolution spectra and we aim to estimate the Hα flux for computing the Hα equivalent width (EW(Hα); see Sect. 6.1), we fixed the [NII]λ6584/Hα line ratio to either the value measured in the corresponding G235M/F170LP data from the same shutter (if detected) or to that measured in the G235M/F170LP data from the adjacent shutter. The [OII]$\lambda\lambda$3727,29 and the [SII]$\lambda\lambda$6716, 31 line doublets are also unresolved in the PRISM spectra. For simplicity, we fit each doublet with a single Gaussian component.

Following all the prescriptions above, we perform the spectral fitting using the python package LMFIT, which delivers the best-fit values of the amplitude, line width, and velocity of each emission line, which minimize the χ^2. In Fig. A.1, we show all PRISM spectra available along with their best-fit model, given by the sum of the continuum model obtained with pPXF and Gaussian emission lines from LMFIT. Stellar continuum and emission lines are detected in all spectra but the External-SE shutter (in pink in Fig. 2), where only continuum emission is detected. To accurately estimate line fluxes and errors, we follow a Monte Carlo approach. Therefore, we perturb the observed spectrum with its associated noise spectrum (from the "error" extension of the data) and repeat the emission-line fitting 200 times, with the line setting described above. In Table A.1, we report the median flux value and the 1σ uncertainty obtained via a Monte Carlo technique for all emission lines detected with a $S/N > 3$.

A.2. Medium- and high-resolution spectra

Following slightly different prescriptions, we fit the medium- and high-resolution spectra (each grating separately). Unlike in the PRISM data, continuum emission is only barely detected in $R = 1000$ and $R = 2700$ data, and does not show significant stellar features to require accurate modeling with SSPs. Therefore, there is no need to use pPXF, and directly perform the emission line modeling with LMFIT, including a second-order polynomial to reproduce the faint detected continuum emission. Since the spectral resolution has a smaller variation with wavelength in the medium- and high-resolution grating (see Jakobsen et al. 2022) (also because each grating covers a total smaller wavelength range), we constrain all lines within the same grating to have the same velocity and velocity dispersion. We still fix the flux ratios of the [NII] and [OIII] line doublets to the theoretical ratios, whereas we fit each line of the [SII]$\lambda\lambda$6716, 31 doublet with two separate Gaussian components, since the two lines are here resolved. The [OII]$\lambda\lambda$3727,29 line doublet, unfortunately, falls into the detector gap of the G140M/F070LP data; hence it is not detected. As for the PRISM data, in Table A.1 we report the median flux values and the 1σ errors for each emission line with a $S/N > 3$, as resulting from a Monte Carlo simulation.

Given that the velocity dispersion measured for K20-ID7 ranges from 20 to 140 km s^{-1} (see Förster Schreiber et al. 2018, Pulsoni et al. in prep), the lines remain spectrally unresolved in the medium-resolution data at $R \sim 1000$ (corresponding to a FWHM of $\sim$ 300 km/s) but are resolved at $R \sim 2700$. Table A.1 lists their intrinsic velocity dispersions, derived after correcting the observed values for instrumental resolution.

Appendix B: Resolved SED best models

Figure B.1 shows the observed SEDs and the best-fit models, resulting from our resolved SED fitting with CIGALE (performed in Sect. 4.1), for four individual pixels representative of distinct galaxy regions (top and middle panels), namely: Clump-N (or Clump A), the bulge, the spiral arm and the inter-arm region southeast and north of the bulge, respectively. Bottom panels show the best fits of the integrated SED modeling (obtained in Sect. 4.3), including photometry up to NIRCam F444W (left) and ALMA Band 6 1.2 mm (right).

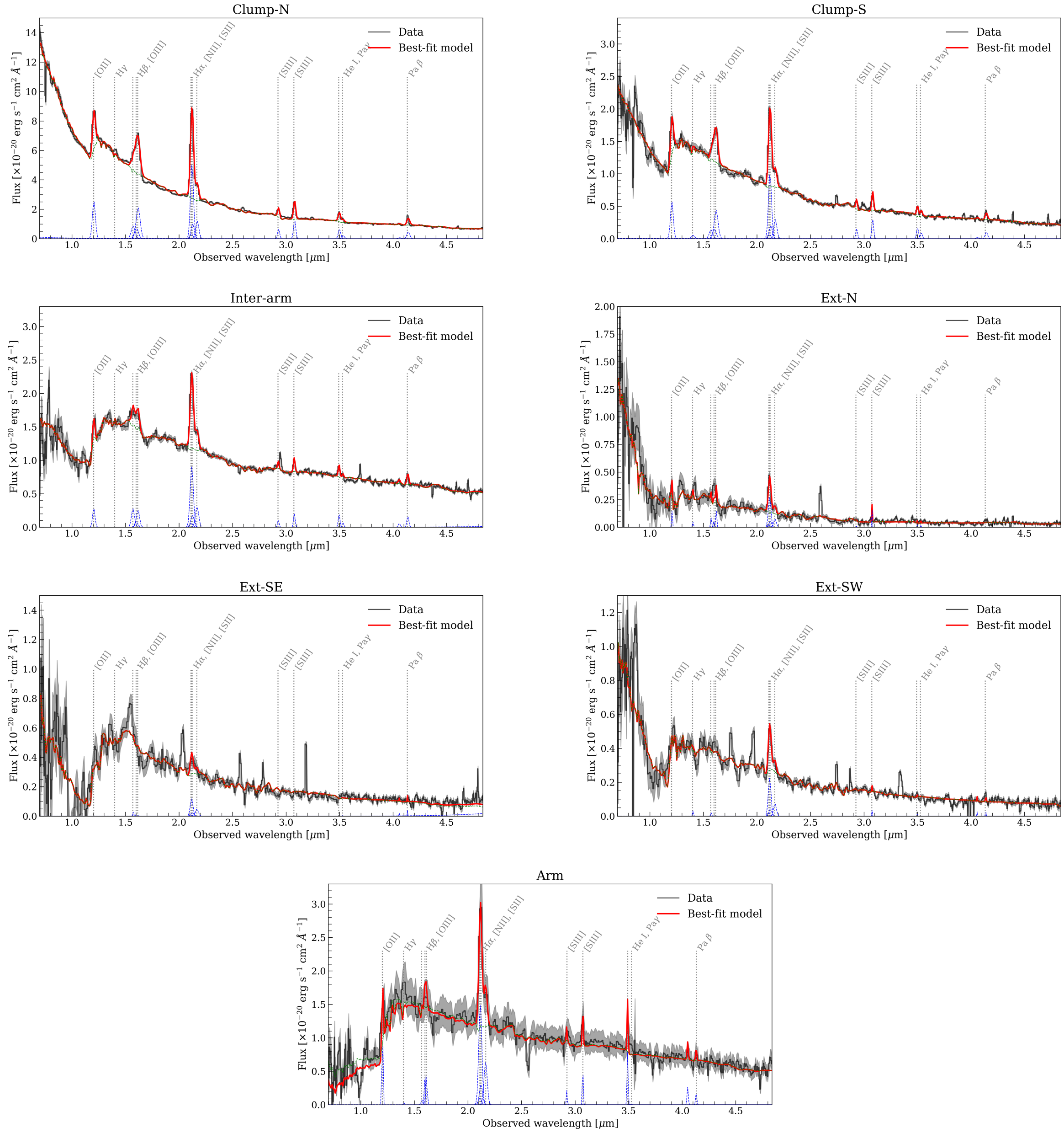

Fig. A.1. NIRSpec MSA PRISM/CLEAR spectra ($R = 100$) of K20-ID7, from all six shutters. Data are shown in black, with the best-fit model overplotted in red. All spectra exhibit both stellar continuum and emission lines, except for the External-SE spectrum, where we only detect continuum emission.

Appendix C: Nebular A_V from NIRCam imaging

In addition to the stellar $A_{V,\rm star}$ map inferred from SED fitting in Sect. 4, we derive an independent map of nebular $A_{V,\rm neb}$ from Paβ/Hα ratios, as inferred by combining available medium-band NIRCam imaging containing Hα and Paβ (i.e., F210M and F410M, respectively), and broadband NIRCam filters (see also Lorenz et al. 2025). We first fit a third-degree polynomial to the broadband photometry of each pixel, considering only filters at longer wavelengths than the Balmer break (i.e., F150W, F200W, F277W, F356W, and F444W), to derive the continuum emission. In the polynomial fitting, we assigned a small uncertainty (i.e., 1%) to the flux of filters with no significant line emission. For the F200W and F444W filters, we assigned larger uncertainties of 10% and 5%, respectively, to account for the contribution of Hα and Paβ emission lines to the total broadband emission. Then, we convolve the continuum best-fit model of each pixel with the F210M and F410M filter transmission, respectively, and integrate the convolved continuum model over the wavelength range of the corresponding filter, thus separately obtaining the contribution of continuum emission to the F210M and F410M bands. By removing the inferred continuum level from the total observed F210M and F410M flux in each pixel, we end up with residual line emission, including also contributions from emission lines other than Hα and Paβ. In particular, line emission of K20-ID7 in the F210M and F410M filters is mostly due to Hα+[NII] and Paβ+[FeII], respectively. Therefore, to obtain an estimate of the Hα and Paβ fluxes only, we correct the resulting total line fluxes by adopting Hα/[NII] and Paβ/[FeII] line ratios, as measured from the MSA spectra. In particular, for the northern clumps (i.e., Clump-N and the smaller northernmost clump) we adopt the flux measurements obtained

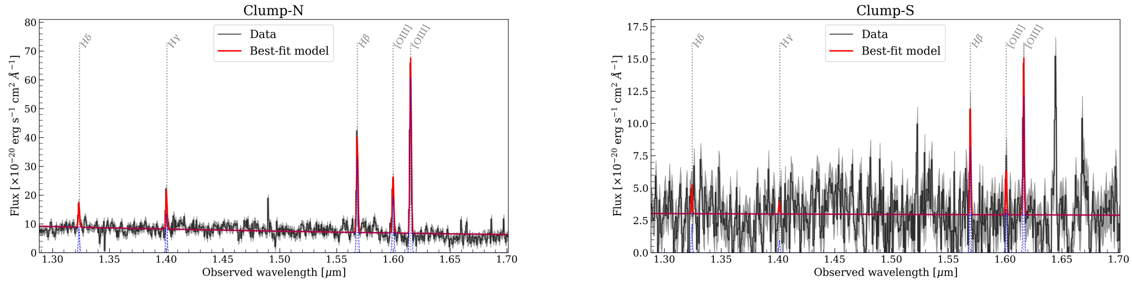

Fig. A.2. NIRSpec MSA medium-resolution spectra ($R = 1000$) of K20-ID7, obtained with the G140M/F070LP grating, for the shutters where we detect emission lines at S/N>3. Data are shown in black, with the best-fit model overplotted in red.

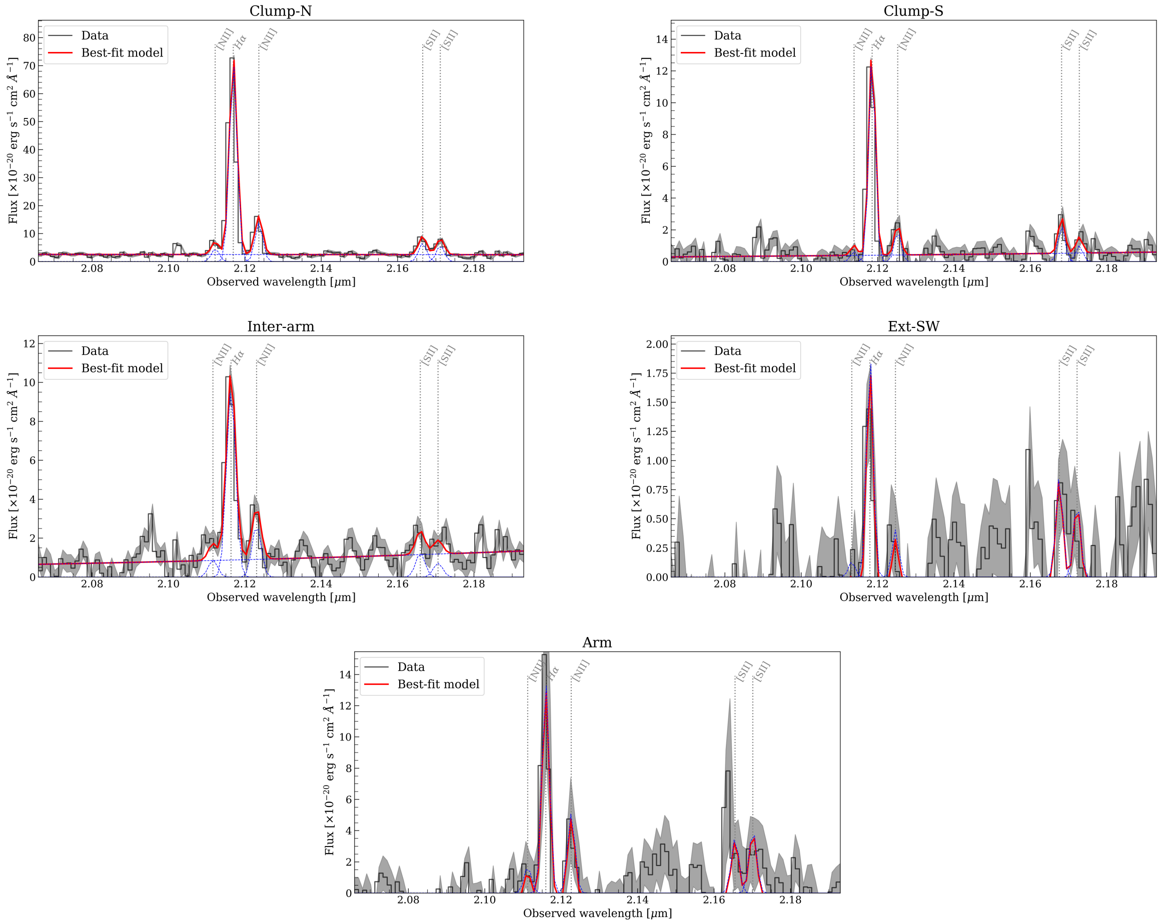

Fig. A.3. NIRSpec MSA medium-resolution spectra ($R = 1000$) of K20-ID7, obtained with the G235M/F170LP grating around the Hα, [NII] complex for the shutters where we detect emission lines at S/N>3. Data are shown in black, with the best-fit model overplotted in red.

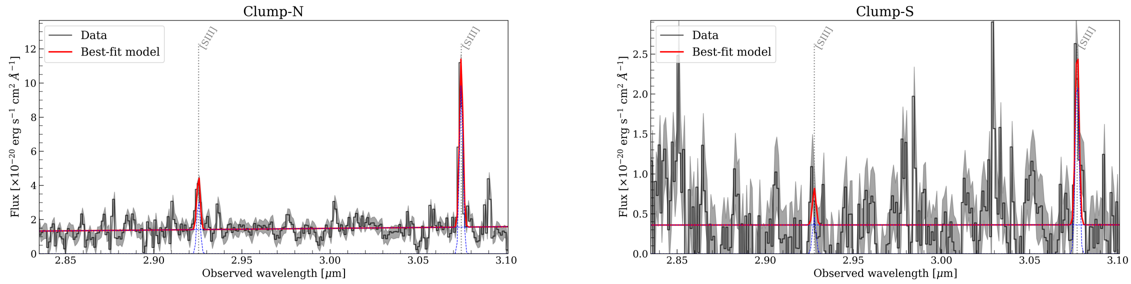

Fig. A.4. NIRSpec MSA medium-resolution spectra ($R = 1000$) of K20-ID7, obtained with the G235M/F170LP grating around the [SIII] emission lines for the shutters where we detect emission lines at S/N>3. Data are shown in black, with the best-fit model overplotted in red.

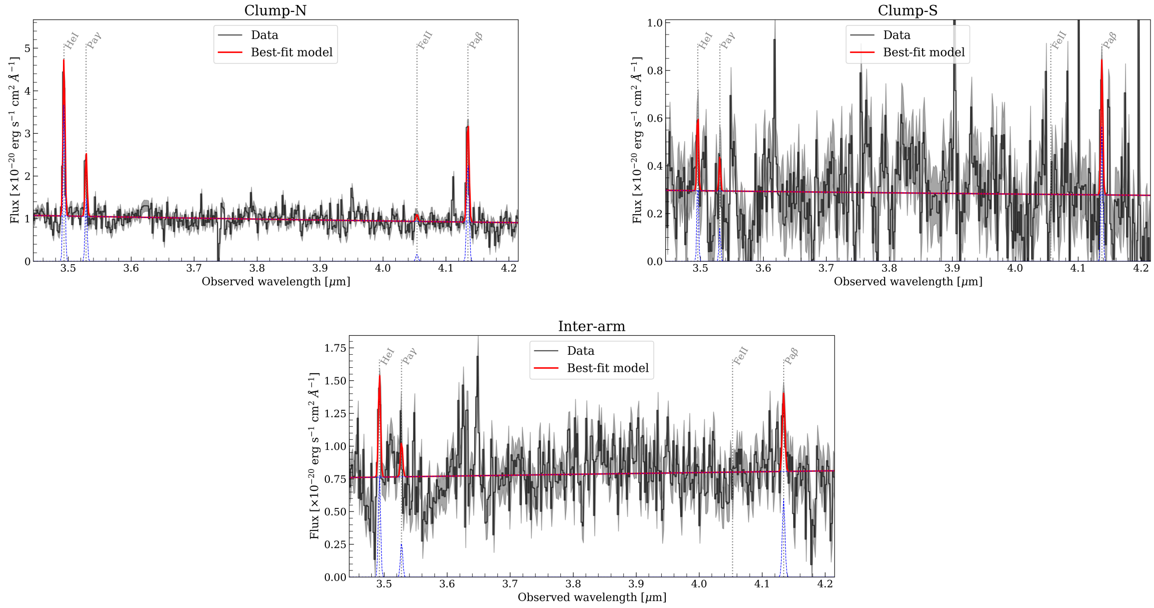

Fig. A.5. NIRSpec MSA high-resolution spectra ($R = 1000$) of K20-ID7, obtained with the G395M/F290LP, for the shutters where we detect emission lines at S/N>3. Data are shown in black, with the best-fit model overplotted in red.

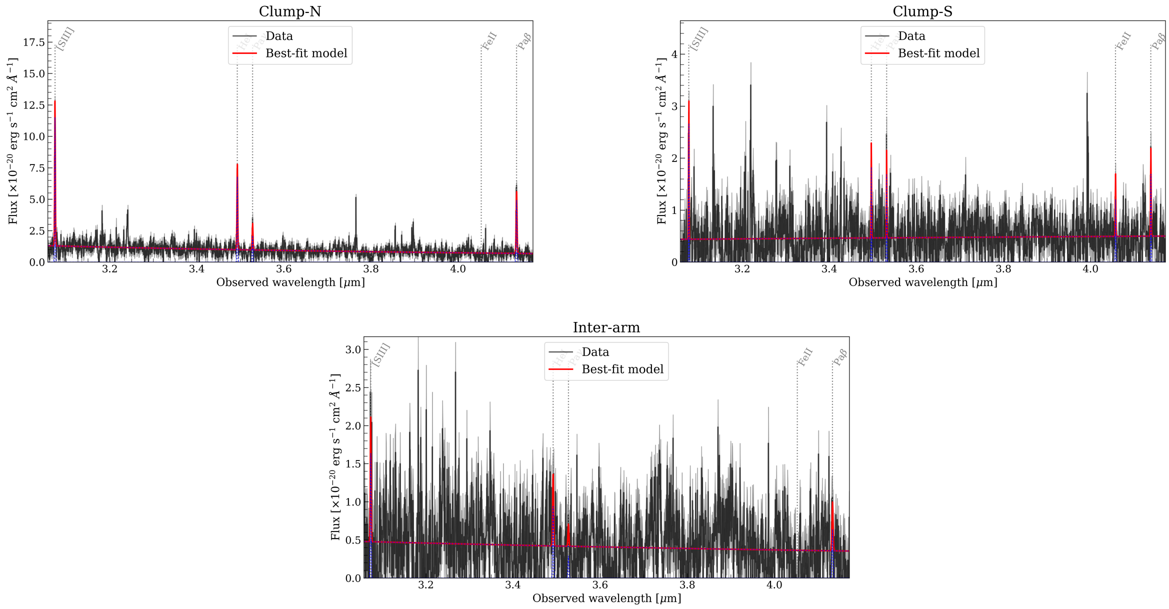

Fig. A.6. NIRSpec MSA high-resolution spectra ($R = 2700$) of K20-ID7, obtained with the G395H/F290LP, for the shutters where we detect emission lines at S/N>3. Data are shown in black, with the best-fit model overplotted in red.

for Clump-N (Hα/[NII] = 5.1 and Paβ/[FeII] = 14); while for all the rest of the galaxy (i.e., spiral arms, inter-arm regions, and bulge), we rely on the line ratios inferred for the Inter-Arm and/or Arm region, when available (i.e., Paβ/[FeII] = 8.4 from Inter-Arm spectra; Hα/[NII] = 3.0, computed as average between line ratios measured from the Inter-Arm and Arm regions).

In Fig. C.1, we show the resulting maps of observed (i.e., not dust corrected) Hα and Paβ flux, along with the nebular $A_{V,\rm neb}$ map, as obtained from pixel-per-pixel Paβ/Hα line ratios, according to a Calzetti et al. (2000) dust attenuation law ($R_V = 4.05$). Unfortunately, due to faintness of the Paβ line emission compared to the continuum, this approximate procedure allows us to recover only Paβ line flux in part of the most actively star-forming regions (i.e., clumps and spiral arms). Apparently Paβ is also detected in the bulge, as opposed to the NIRCam WFSS Paβ map (shown in Fig. 5). For this reason, we caution on the reliability of the Paβ detection in the inner central regions. The right-hand panel of Fig. C.1 displays the resulting $A_{V,\rm neb}$ map inferred from Paβ/Hα line ratios, after masking pixels with (non-physical) negative $A_{V,\rm neb}$ values. Due to the sparse $A_{V,\rm neb}$ map, we estimated the average $A_{V,\rm neb}$ value after masking pixels within the 0.25″-diameter bulge aperture (subjected to the large uncertainties in the Paβ line flux). We adopted this value as the global dust attenuation of the galaxy, assuming an uncertainty of 30% (i.e., $A_{V,\rm neb} = 2.0 \pm 0.6$).

Table A.1. Best-fit results for emission lines detected at S/N > 3 in the NIRSpec MSA spectra of K20-ID7 at different spectral resolution.

Line	PRISM/CLEAR						G140M/F070LP, G235M/F170LP, G395M/F290LP (G395H/F290LP)				
	Arm	Inter-Arm	Clump-N	Ext-N	Clump-S	Ext-SW	Arm	Inter-Arm	Clump-N	Clump-S	Ext-SW
[OII]$\lambda\lambda$3727,29	-	85 ± 33 $^{(*)}$	917 ± 43 $^{(*)}$	-	184 ± 34 $^{(*)}$	-	-	-	-	-	-
Hδ	-	-	-	-	-	-	-	-	111 ± 14	-	-
Hγ	-	-	20 ± 1	-	-	-	-	-	191 ± 16	-	-
Hβ	-	-	380 ± 31	-	-	-	-	-	525 ± 18	102 ± 15	-
[OIII]λ5007	-	-	997 ± 35	-	192 ± 24	-	-	112 ± 23	972 ± 18	155 ± 17	-
Hα	606 ± 190	350 ± 16	1782 ± 22	83 ± 14	355 ± 13	65 ± 10	332 ± 45	293 ± 13	1792 ± 12	281 ± 10	41 ± 10
[NII]	-	70 ± 4	357 ± 4	-	71 ± 3	-	136 ± 40	82 ± 10	351 ± 9	40 ± 9	-
[SII]λ6717	-	122 ± 19 $^{(*)}$	424 ± 20 $^{(*)}$	-	108 ± 15 $^{(*)}$	-	-	37 ± 11	171 ± 9	47 ± 10	-
[SII]λ6731	-	-	-	-	-	-	-	24 ± 11	148 ± 10	20 ± 9	-
[SIII]λ9069	-	-	153 ± 9	-	30 ± 7	-	-	-	76 ± 8	-	-
[SIII]λ9533	-	34 ± 12	325 ± 10	-	61 ± 9	-	-	-	249 ± 8	65 ± 15	-
	-	-	-	-	-	-	-	(39 ± 5)	(218 ± 6)	(33 ± 4)	-
HeIλ1.083	-	41 ± 10	175 ± 7	-	40 ± 6	-	-	33 ± 6	146 ± 5	11 ± 4	-
	-	-	-	-	-	-	-	(24 ± 5)	(144 ± 6)	(24 ± 6)	-
Paγ	-	-	60 ± 6	-	20 ± 4	-	-	-	59 ± 4	-	-
	-	-	-	-	-	-	-	-	(46 ± 5)	(22 ± 3)	-
Paβ	-	35 ± 7	151 ± 7	-	29 ± 5	-	-	30 ± 6	112 ± 4	22 ± 5	-
	-	-	-	-	-	-	-	(20 ± 5)	(127 ± 5)	(26 ± 4)	-
σ_{gas}	-	-	-	-	-	-	-	(79 ± 10)	(55 ± 2)	(44 ± 3)	-

Notes. All fluxes are in units of 10^{-20} erg s^{-1} cm^{-2}. For the reddest G395M and G395H gratings, we provide line fluxes measured at both medium and high spectral resolution (the latter in brackets). The last row reports the intrinsic velocity dispersion σ_{gas} (i.e., corrected for instrumental broadening) in units of km s^{-1}, as measured in high-resolution G395H data. $^{(*)}$ Total fluxes computed as the sum of the flux of the two [OII]$\lambda\lambda$3727,29 and [SII]$\lambda\lambda$6716, 31 doublet components, which are unresolved in PRISM/CLEAR spectra ($R = 100$).

Appendix D: Validating resolved SED fitting results

To check on the reliability of the results of our spatially resolved SED fitting, we recover the expected observed Hα flux by combining the SFR10 and $A_{V,\rm star}$ maps. As we discussed in Sects. 5-6, nebular line emission is expected to be subject to extra attenuation compared to the stellar populations in regions of intense star formation (e.g., Calzetti et al. 2000; Price et al. 2014; Tacchella et al. 2018). Therefore, as a first approximation, we used the $A_{V,\rm star}$ map – the only full A_V map available – while acknowledging that it may locally underestimate the true attenuation of the Hα line emission. In particular, we first convert the SFR10 into Hα intrinsic luminosity according to the Kennicutt & Evans (2012) relation, which is in turn converted into the observed Hα flux by (de-)correcting for dust attenuation (Calzetti et al. 2000) law, using the $A_{V,\rm star}$ values previously inferred for each single pixel. In Fig. D.1 we show the comparison of our recovered observed Hα flux (left-hand panel) with the real observed one from ERIS observations (right-hand panel, same color scale; Forster Schreiber The two Hα maps overall show a good agreement, especially in correspondence of the two northern Hα-bright clumps (i.e., Clumps A and B), while the similarity is less evident in the regions of fainter Hα emission, due to the lower S/N of ERIS data. However, the ERIS Hα map displays increased emission at the southernmost clump (Clump C), and along the spiral arm east of the bulge. The overall good similarity between the two Hα maps points to the reliability of our SFR10 map, although some degeneracy might still be present between SFR10 and $A_{V,\rm star}$ values for a given observed Hα flux. By summing over all pixels, we obtain a total recovered Hα flux of 2.0×10^{-16} erg s^{-1} cm^{-2}, which is consistent with the total Hα flux measured from ERIS and SINFONI data (Förster Schreiber et al. 2009). We note that, although in principle it is possible to insert as input in `CIGALE` also emission-line fluxes, we do not do it because of the difficulties in correctly aligning (on a pixel level of 0.025″) the NIRCam, ACS, and ERIS data. This test highlights that we are able not only to correctly recover the total Hα flux, but also its spatial distribution, showing the reliability of our spatially resolved SED analysis.

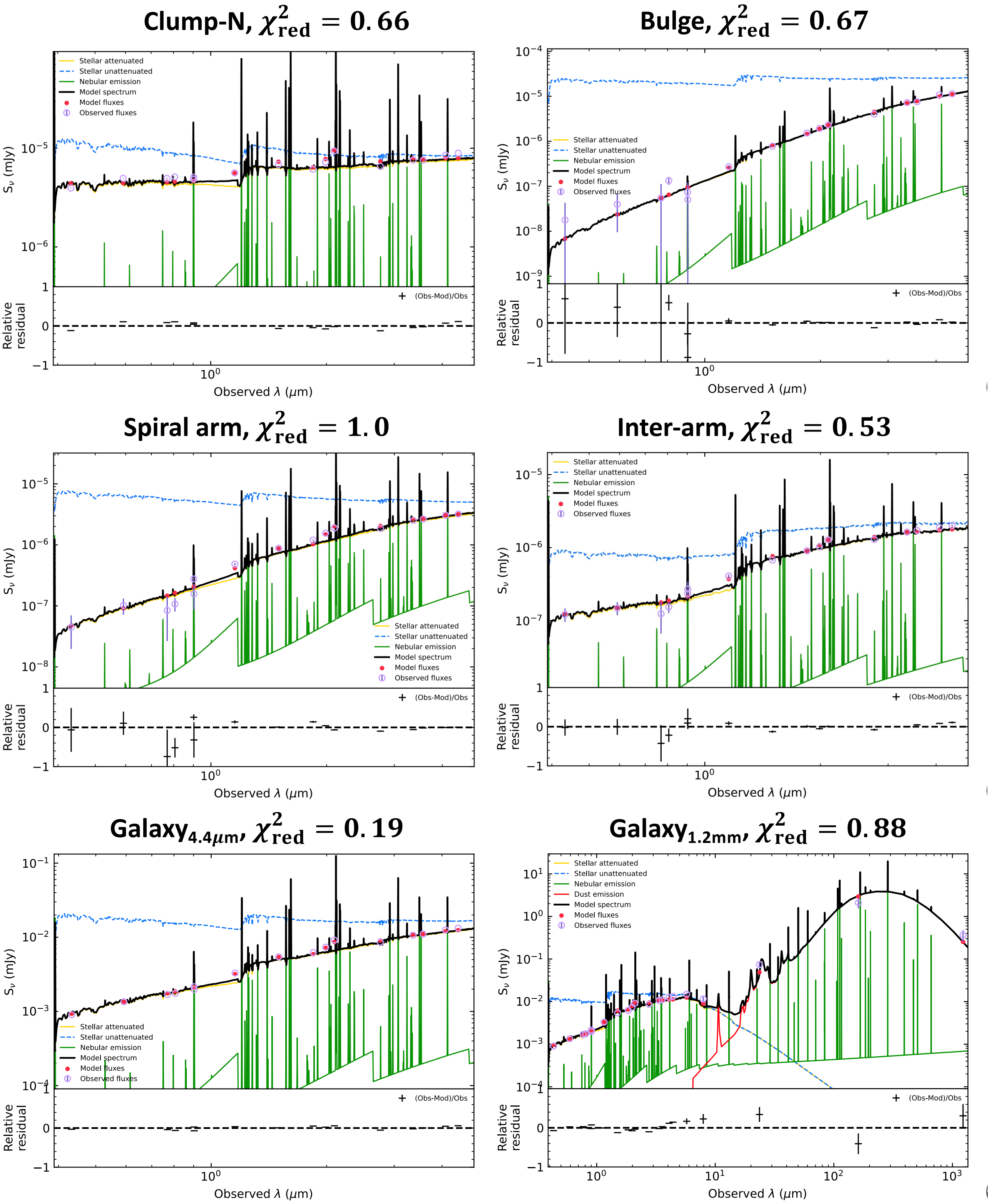

Fig. B.1. Best-fit models and observed SEDs as obtained from our resolved (top and middle panels) and integrated (bottom) SED modeling with `CIGALE`. *Top and middle.* Resolved results are shown for four representative pixels from four different regions, namely: Clump-N, the bulge, spiral arm, and inter-arm regions. The difference in the SED shape and in the relative intensities between distinct spectral components highlights the need for spatially resolved SED fitting to accurately account for the different physical properties of distinct galaxy regions. *Bottom.* Results from our integrated SED modeling of photometry up to 4.4 μm (left) and 1.2 mm (right), respectively.

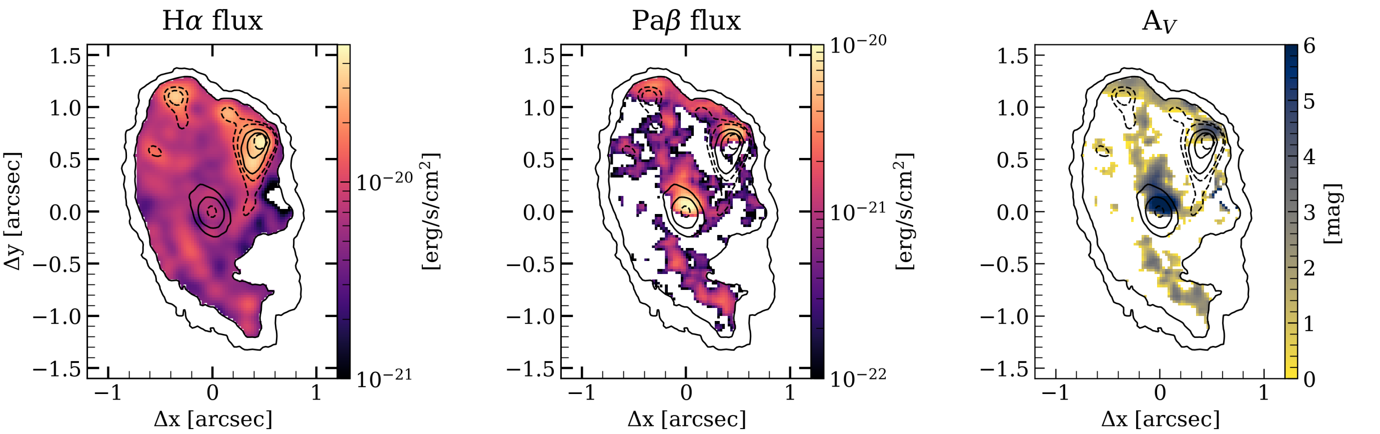

Fig. C.1. Line emission from medium-band F210M and F410M NIRCam imaging. From the left, we show maps of recovered Hα and Paβ line flux (not corrected for dust attenuation), and finally of nebular A_V, as inferred from Paβ/Hα line ratios. The solid and dashed black contours are the same as in Fig. 4.

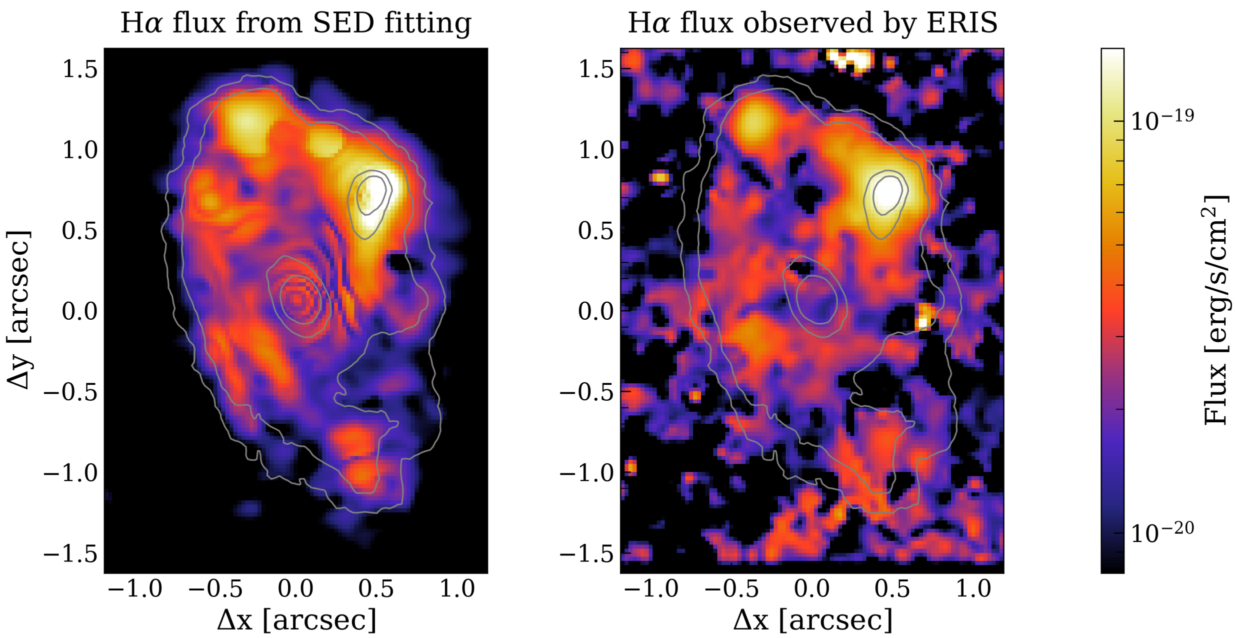

Fig. D.1. Expected observed Hα flux (left), as recovered from the SFR10 and $A_{V,\mathrm{star}}$ maps resulting from our spatially resolved SED fitting (see Fig. 4), and the real observed Hα flux from VLT/ERIS observations (right). The gray contours trace NIRCam F444W emission at 5%, 10%, 35%, 50% of the emission peak. Both maps have the same color scale and a 0.025″ pixel scale.